Scalco, M, Gerasimov, R, Bedin, LR, Vesperini, E, Nardiello, D, Libralato, M, Burgasser, A, Griggio, M, Bellini, A, Anderson, J, Salaris, M, Apai, D and Häberle, M

JWST imaging of omega Centauri I. Luminosity and mass functions of its main-sequence populations

A&A, 701, A169 (2025)
https://doi.org/10.1051/0004-6361/202555452

Astronomy & Astrophysics

JWST imaging of omega Centauri

I. Luminosity and mass functions of its main-sequence populations

M. Scalco[1,⋆], R. Gerasimov[2], L. R. Bedin[3], E. Vesperini[1], D. Nardiello[4,3], M. Libralato[3], A. Burgasser[5], M. Griggio[6], A. Bellini[6], J. Anderson[6], M. Salaris[7,8], D. Apai[9,10], and M. Häberle[11]

[1] Department of Astronomy, Indiana University, Swain West, 727 E. 3rd Street, Bloomington, IN 47405, USA
[2] Department of Physics and Astronomy, University of Notre Dame, Nieuwland Science Hall, Notre Dame, Indiana 46556, USA
[3] Istituto Nazionale di Astrofisica, Osservatorio Astronomico di Padova, Vicolo dell'Osservatorio 5, Padova I-35122, Italy
[4] Dipartimento di Fisica e Astronomia "Galileo Galilei", Università di Padova, Vicolo dell'Osservatorio 3, Padova I-35122, Italy
[5] Department of Astronomy & Astrophysics, University of California, San Diego, La Jolla, California 92093, USA
[6] Space Telescope Science Institute, 3700 San Martin Drive, Baltimore, MD 21218, USA
[7] Astrophysics Research Institute, Liverpool John Moores University, 146 Brownlow Hill, Liverpool L3 5RF, UK
[8] Istituto Nazionale di Astrofisica, Osservatorio Astronomico d'Abruzzo, Via Mentore Maggini, Teramo I-64100, Italy
[9] Department of Astronomy and Steward Observatory, The University of Arizona, 933 N. Cherry Avenue, Tucson, AZ 85721, USA
[10] Lunar and Planetary Laboratory, The University of Arizona, 1629 E. University Blvd., Tucson, AZ 85721, USA
[11] Max Planck Institute for Astronomy, Königstuhl 17, D-69117 Heidelberg, Germany

Received 8 May 2025 / Accepted 31 July 2025

ABSTRACT

This paper presents the first study of the most massive globular cluster in the Milky Way, omega Centauri (or ω Cen, also known as NGC 5139), employing recently acquired JWST deep images. By combining these data with archival *Hubble* Space Telescope (HST) images, we derived proper motions for a significant portion of the JWST field. Our analysis of the colour-magnitude diagram (CMD) reveals two prominent sequences extending from a magnitude of $m_{\rm F322W2} \sim 17.5$ to the bottom of the main sequence (MS). These sequences correspond to the two main stellar populations of omega Centauri: the bMS (He-rich) and rMS (He-normal) populations. The two sequences intersect at the MS knee ($m_{\rm F322W2} \sim 19.5$) and change positions for fainter magnitudes, with the bMS luminosity function (LF) ending at least ~0.5 magnitudes brighter than the rMS LF. Our comparison with theoretical isochrones shows that the colour spread in the CMD is primarily driven by variations in the helium abundance above the MS knee, while below the MS knee the broader colour distribution is mainly influenced by variations in oxygen and carbon abundances, in combination with metallicity differences. We find that a single-population broken power-law mass function (MF) provides the best fit to the data. The MF exhibits a break around 0.2 $M_\odot$, with a steep slope above the break and a flatter slope below it. Finally, we identified a third group of stars (named gMS) along the MS located between the two primary ones and conducted a detailed analysis of the LFs and MFs for these three stellar populations. The LFs of these sequences show similar trends, with the rMS being the most populated and the bMS the least. The MFs display distinct power-law slopes: the rMS is well fitted by a single power law, while the gMS and the bMS are characterised by MFs steeper than that of the rMS for masses larger than 0.2 $M_\odot$ and flatter MFs for smaller masses. The flattening around ~0.2 $M_\odot$ for the gMS and the bMS might be a real feature of the MFs of these populations or due to uncertainties in the adopted mass-luminosity relationship. The variation in the slope of the MFs of the gMS and bMS contributes to the steepening (flattening) of the combined MF for masses higher (lower) than 0.2 $M_\odot$.

Key words. proper motions – stars: luminosity function, mass function – globular clusters: individual: NGC 5139

1. Introduction

Globular clusters (GCs), comprising the oldest and largest coeval stellar populations, serve as crucial markers for the chemical evolution of the Galaxy and provide valuable insights into the nature of ancient metal-poor stars. The long-standing belief that all stars within a cluster have the same chemical composition was challenged by spectroscopic studies, which revealed the presence of chemical inhomogeneities in some clusters (see e.g. Gratton et al. 2012, and references therein). Two decades of space-based photometric studies have further revolutionised our understanding of GCs, uncovering intricate colour-magnitude diagrams (CMDs) that reveal the presence of multiple stellar populations (mPOPs) with varying chemical compositions. Despite these discoveries, the process driving this chemical diversity remains unclear, partly because most research on GCs has focused on the brighter stars, such as those on the upper main sequence (MS) or in the giant phase (see Bastian & Lardo 2018; Gratton et al. 2019, for a recent review).

In this paper, we present JWST images of NGC 5139 (hereafter referred to as ω Cen), the relatively close (we assumed the distance of 5.24±0.11 kpc from Soltis et al. 2021, throughout the paper) and most massive (~4×10^6 $M_\odot$; Giersz & Heggie 2003; D'Souza & Rix 2013) GC in the Milky Way. These observations aim to investigate the faintest objects within the cluster using near-infrared (NIR) data and explore the mPOPs in the faintest regions of its CMD.

⋆ Corresponding author: mscalco@iu.edu

ω Cen is well known for its complex mPOP system, making it one of the most enigmatic stellar systems in the Galaxy. It hosts at least two main stellar components: the blue main sequence (bMS) and the red main sequence (rMS) (e.g. Bedin et al. 2004), with the bMS more centrally concentrated than the rMS (Bellini et al. 2009; Sollima et al. 2007a). Except for the cluster's central region, the rMS is the dominant population. This initially appeared inconsistent with spectroscopic studies, which indicated that lower-metallicity stars are the most abundant in the cluster (e.g. Norris & Da Costa 1995). To resolve this discrepancy, Bedin et al. (2004) proposed that the bMS might be significantly more enhanced in helium than the rMS. This hypothesis was supported by Norris (2004), who estimated a helium mass fraction difference of $\Delta Y \sim 0.12$ between the two sequences. Further confirmation came from Piotto et al. (2005), who demonstrated that bMS stars are indeed more metal-rich than their rMS counterparts by ∼0.3 dex, while King et al. (2012) derived a helium mass fraction of $Y = 0.39 \pm 0.02$ for the bMS. However, a more recent spectroscopic analysis by Latour et al. (2021) based on MUSE data suggests a smaller helium difference between the bMS and rMS ($Y \lesssim 0.1$).

Another remarkable feature of ω Cen is the unusually broad metallicity spread observed within each sequence, significantly larger than what is typically found in other GCs. The metallicity ranges from [Fe/H] ≈ −2.2 to −0.5, with [X/Fe] dispersions reaching 0.5 to more than 1.0 dex for several elements (e.g. Norris & Da Costa 1995; Suntzeff & Kraft 1996; Smith et al. 2000; Johnson et al. 2008, 2009; Bellini et al. 2017a). This suggests that ω Cen might be the nucleus of a dwarf galaxy absorbed by the Milky Way, or the outcome of the merger of two or more clusters (Norris et al. 1997; Jurcsik 1998; Bekki & Freeman 2003; Pancino et al. 2000; Bekki & Norris 2006; Ibata et al. 2019; van de Ven et al. 2006). Recent studies have further revealed that both the bMS and rMS are subdivided into multiple subpopulations, with up to 15 distinct stellar populations identified within the cluster so far (Bellini et al. 2017a; Scalco et al. 2024a).

The high-resolution deep NIR images provided by JWST have proven to be very effective in the exploration of mPOPs in GCs (47 Tuc; Milone et al. 2023; Marino et al. 2024, M92; Nardiello et al. 2022, NGC 6440; Cadelano et al. 2023 and NGC 6397; Scalco et al. 2024b). Here, we present the first[1] analysis of the mPOPs in ω Cen using JWST photometry, with a focus on their luminosity function (LF) and mass function (MF) along the MS.

The paper is organised as follows. Section 2 describes the data and reduction methods, while Section 3 focuses on the evaluation of proper motions (PMs). Section 4 presents the CMD of ω Cen based on JWST photometry, followed by Section 5, which details the artificial star (AS) tests. Section 6 analyses the LFs and MFs of ω Cen and its stellar populations using JWST data. Finally, a brief summary is provided in Section 7.

2. Observations and data reduction

The data analysed in this study were obtained from two programmes:

– Our proprietary images from JWST GO-5110 programme (Bedin et al. 2024a). The JWST data were obtained with the Near Infrared Camera (NIRCam, Rieke et al. 2023) simultaneously with the Short Wavelength (SW) and Long Wavelength (LW) channels on August 7–8, 2024 (epoch ∼2024.6). Ultra-wide filters were used for both NIRCam channels: F150W2 for the SW channel and F322W2 for the LW channel. The six-point `FULLBOX` primary pattern was employed with a `THREE-POINT-LARGE-WITH-NIRISS` sub-pixel dither pattern. At each of the resulting 18 pointings, a single image was captured in both channels using the `MEDIUM8` readout pattern (nine groups), resulting in an effective exposure time of 944.836 s per image.

– Archival material from our HST GO-14118+14662 (Bedin et al. 2016a,b) multi-epoch programme. This dataset includes images taken with the Wide Field Channel (WFC) of the Advanced Camera for Surveys (ACS) using the F606W and F814W filters, spanning a period from ∼2015.6 to ∼2018.5. These data were reduced and presented in a recent paper by Scalco et al. (2024c), where a comprehensive description of the dataset can be found.

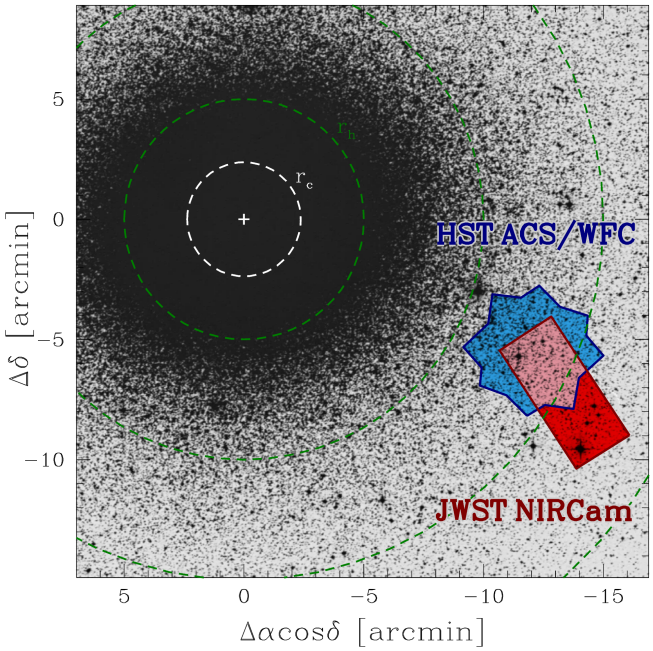

Fig. 1. NIRCam JWST field from the GO-5110 programme (red) and the ACS/WFC HST field from the GO-14118+14662 programme (blue) overlaid on a DSS image of ω Cen. The overlap region between the two datasets is highlighted in magenta. Units are in arcminutes from the cluster's centre. The dashed white and green circles represent the core radius (r_c = 2′.37) and the half-light radius (r_h = 5′.00), respectively, with additional circles marking 2 r_h, 3 r_h, and 4 r_h. The values of r_c and r_h are from Trager et al. (1995), McLaughlin & van der Marel (2005) as reported in the Harris (1996, 2010) catalogue.

Figure 1 shows the positions of our datasets within the field of view (FOV), overlaid on a Digital Sky Survey[2] (DSS) image of ω Cen. The overlapping region between the two datasets, highlighted in magenta, covers a radial range from ∼2.4 r_h to ∼3.2 r_h.

JWST images were processed using the software tools and methods detailed in Papers I, II, and III of the 'Photometry and Astrometry with JWST' series (Nardiello et al. 2022, 2023a; Griggio et al. 2023), which have been successfully applied in recent studies of 47 Tuc by Nardiello et al. (2023b), Scalco et al. (2025). We first processed the level-1b uncalibrated (`_uncal`) images using a development version of the JWST pipeline[3]

[1] After our submission of this paper (on May 8, 2025), a manuscript on the dynamical properties of ω Cen based in part on JWST observations was posted on arXiv (Ziliotto et al. 2025, June 26, 2025).

[2] https://archive.eso.org/dss/dss

[3] https://github.com/spacetelescope/jwst

(Bushouse et al. 2023), running it through stages 1 and 2 to produce the level-2b (_cal) images. In the stage 1 pipeline, we utilised the default parameters with one exception: for the ramp fitting process, we employed the `frame zero` (the initial frame of each integration) to measure pixels that were saturated in the first group and extended up to the ramp. This approach effectively increased the dynamic range of our data by almost two magnitudes, extending into the nominally saturated intensity regime. The stage 2 pipeline was executed with all default parameters.

The reduction of the _cal images involved two main steps: first-pass and second-pass photometry. In the first-pass, starting from the empirical library point spread function (PSF) derived in Bedin et al. (2024b), we extracted PSFs, positions, and magnitudes of stars from each individual image. A geometric distortion correction was applied to the star positions using the solution by Griggio et al. (2023). The coordinates from each image were then transformed to a common reference frame, with bright cluster members from *Gaia* Data Release 3 (DR3; Gaia Collaboration 2016, 2023) serving as the reference, after transforming their positions to the epoch of the data collection.

For the second-pass photometry, we utilised a modified version of the KS2 code as described in Bellini et al. (2017b, 2018), Nardiello et al. (2018), Libralato et al. (2018, 2022), Scalco et al. (2021) and references therein. In this step, positions and fluxes were extracted using the PSFs and transformations obtained during the first-pass. KS2 processes all images simultaneously, making it well suited for detecting faint sources that may not be visible in individual frames. Along with fluxes and positions, KS2 generates several quality parameters, such as the PSF quality-of-fit (QFIT) parameter, the RADXS parameter (a metric for comparing the shape of a source to the PSF; see Bedin et al. 2008, 2009), and the local sky noise (rmsSKY). Detailed descriptions of these diagnostics can be found in Bellini et al. (2018), Scalco et al. (2021), Nardiello et al. (2018).

We applied a similar reduction process to the HST data, following the same first- and second-pass photometry approach. For a detailed explanation of the HST data reduction, we refer to Scalco et al. (2024c).

We calibrated our HST and JWST photometry to the VEGA-magnitude system following the procedures illustrated in Nardiello et al. (2023a, see also Bedin et al. 2005), while we anchored the astrometry to the International Celestial Reference System (ICRS) frame using *Gaia* DR3 data for sources in the observed fields.

We selected a sample of well-measured stars using the quality parameters provided by KS2 (QFIT, RADXS, and rmsSKY). In particular, we retained sources with `QFIT` > 0 and absolute `RADXS` values smaller than 0.05 in both filters. As for `rmsSKY`, we manually defined a fiducial threshold as a function of magnitude, following the trend of `rmsSKY` with magnitude, and excluded all sources lying above this threshold. Finally, we corrected our photometry for the effects of differential reddening and spatial zero-point variations following the procedure introduced in Sarajedini et al. (2007, see also Milone et al. 2012, Bellini et al. 2017c). Filter-specific extinction coefficients were computed assuming $A_V = 3.1 \times E(B-V)$, with a mean reddening $E(B-V) = 0.12$ (Harris 1996; Calamida et al. 2005). We adopted the extinction ratios for JWST/NIRCam filters from Wang & Chen (2019) ($A_{\rm F150W2} = 0.15 \times A_V$, $A_{\rm F322W2} = 0.04 \times A_V$). The measured differential reddening values $\delta E(B-V)$ range from approximately -0.05 to $+0.04$ across the field. Figure 2 presents the $m_{\rm F150W2}$ versus $m_{\rm F150W2} - m_{\rm F322W2}$ CMD (panel a) and the $m_{\rm F322W2}$ versus $m_{\rm F150W2} - m_{\rm F322W2}$ CMD (panel b) for all stars in the JWST field. In both panels, black dots represent stars passing the photometric quality selections while grey dots represent stars not passing the selections. The black dots distinctly outline the cluster's MS and low-MS, as well as its white dwarf (WD) cooling sequence (CS), located in the bottom-left of the CMDs. In both panels, the light red area indicates the onset of saturation, where photometry is obtained from the `frame zero`. The dark red region marks severe saturation, where even the `frame zero` is affected and the flux must be recovered from the unsaturated wings of the PSF. In this region, the photometry becomes unreliable, with the sequence displaying non-physical features. Both the photometry and the astrometry of stars in these regions must therefore be treated with particular caution. Stars within these saturated regions are not ideal for scientific analysis that require high photometric accuracy – such as the determination of the LFs and MFs of the individual stellar populations (see Section 6.2), which represents the core of this study – and will not be utilised for these purposes. However, for completeness and to provide a comprehensive view of the CMD morphology of ω Cen, we still include and make use of these stars in other parts of the paper. The reader should nevertheless keep in mind that any results involving stars in the saturated regime must be interpreted with appropriate caution.

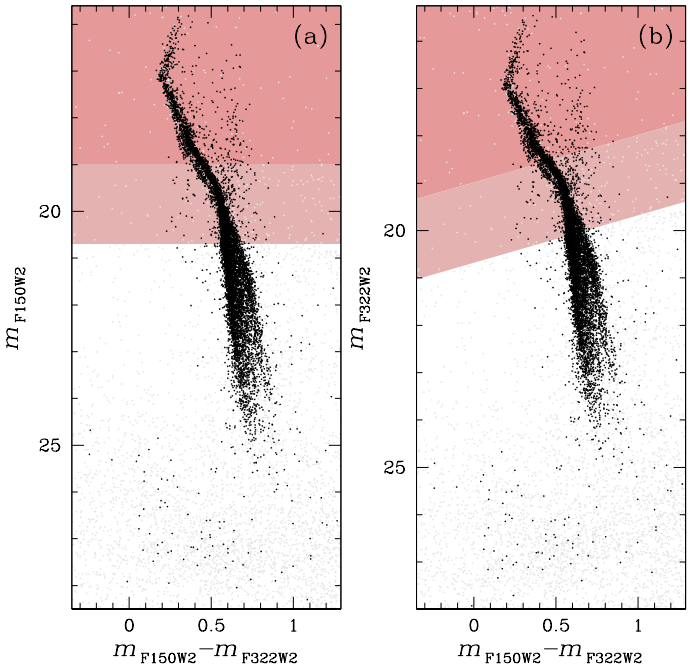

Fig. 2. Colour-magnitude diagrams of ω Cen using JWST filters. (a) $m_{\rm F150W2}$ versus $m_{\rm F150W2} - m_{\rm F322W2}$ CMD. (b) $m_{\rm F322W2}$ versus $m_{\rm F150W2} - m_{\rm F322W2}$ CMD. In both panels, black dots represent stars passing the quality selections while grey dots represent stars not passing the selections. The shaded light red and dark red regions highlight areas of the CMDs affected by saturation. The light red region corresponds to saturated photometry, while the dark red region represents severe saturation, where the photometry is saturated even in the `frame zero`.

Figure 3 shows the same CMDs as in Fig. 2, but limited to stars located in the overlap region between the JWST and HST FOV. While the number of sources is noticeably reduced (by ~30%), the two sequences along the MS remain visible. However, the presence of some contaminants highlights the need for a PM-based cluster membership selection, which will be addressed in the following section.

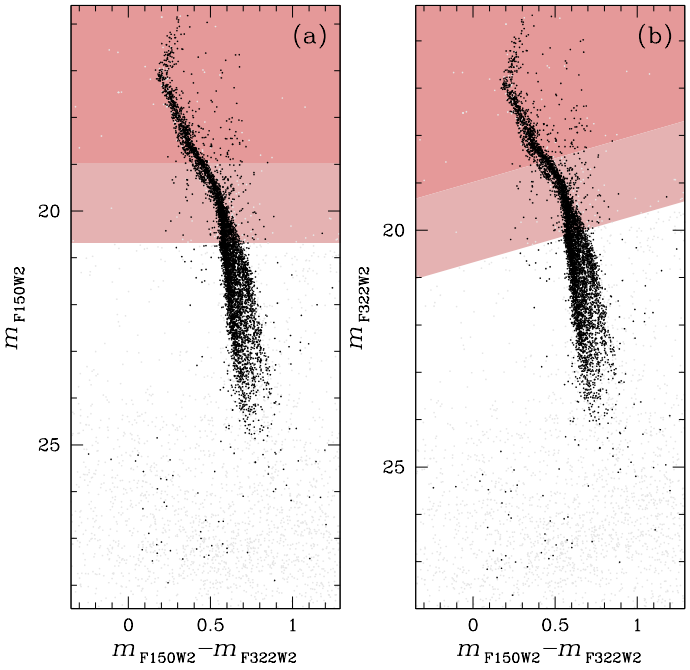

Fig. 3. Same as Fig. 2, but only for the sources located in the overlap region between the JWST and HST FOV.

3. Proper motions

Proper motions (PMs) were computed as displacements between the HST and JWST observations divided by the temporal baseline (~7.5 years). For the HST epoch, we adopted the average position across the available exposures, given the much shorter time span relative to the HST–JWST baseline. The resulting PMs are shown in Fig. 4, which includes only stars that meet the photometric quality criteria described in the previous section and have measurable PMs. Panels (a) and (b) show the vector-point diagram (VPD) and the m_{F322W2} versus $m_{F150W2} - m_{F322W2}$ CMD, respectively. Since PMs are calculated relative to the cluster's overall motion, the distribution of cluster members in the VPD is centred at (0,0). A second, sparser group of points is visible in the upper part of the VPD, representing background and foreground sources. Panel (c) shows the one-dimensional PM (μ_R, obtained by summing the PMs in the two directions in quadrature) plotted against m_{F322W2}. ω Cen members exhibit a narrow distribution in μ_R, mostly clustered below $\mu_R < 2$ mas yr^{-1}, while field objects extend towards higher μ_R. We defined a conservative PM selection to separate cluster members from field objects, indicated by a red line. Panels (d) and (e) show the VPD and m_{F322W2} versus $m_{F150W2} - m_{F322W2}$ CMD for the stars that passed the PM selection, while panels (f) and (g) show the same diagrams for stars that did not pass the PM selection. In panels (b), (e), and (g), the shaded light red and dark red regions indicate areas of the CMDs affected by mild and severe saturation, respectively. The PMs of stars in these regions should be treated with caution. In what follows, our analysis will focus exclusively on the sample of stars shown in panels (d) and (e).

4. The JWST colour-magnitude diagram of ω Cen

In the CMDs presented in Figs. 2, 3 and 4, the MS appears to be composed of two distinct components, which are clearly visible in the magnitude range from $m_{F150W2} \sim 18$ ($m_{F322W2} \sim 17.5$) down to $m_{F150W2} \sim 20$ ($m_{F322W2} \sim 19.5$). At this point, the two sequences intersect and exchange positions. The sequence that is bluer above the intersection (and redder below) corresponds to the bMS population, while the sequence that is redder above the intersection (and bluer below) corresponds to the rMS population.

Note that we have chosen to maintain the names – bMS and rMS – as they were originally introduced based on the identification of these sequences using optical filters, where the bMS appears on the blue side and the rMS on the red side of the CMD (see Bedin et al. 2004; Bellini et al. 2009). Although in the low-MS, which is the focus of our study, the two sequences appear inverted in the JWST CMD (with the rMS on the blue side and the bMS on the red side), we retain this nomenclature for consistency with previous works.

To illustrate this inversion, in Fig. 5, we have isolated a sample of bMS and rMS stars from the CMD based on optical HST photometry and shown their position on the JWST CMD. As clearly shown, the bMS crosses the rMS around $m_{F150W2} \sim 20$, becoming redder at fainter magnitudes. Below this crossing point, rMS stars span a broad colour range, but their distribution appears to favour bluer colours.

We note that, despite the onset of saturation at $m_{F150W2} \sim 20.7$, the two MSs remain clearly distinguishable in the JWST CMD, with a colour separation that appears well defined throughout the saturated regime. Although saturation introduces photometric discontinuities, it affects both sequences in a similar way and does not prevent a qualitative assessment of their morphology in this region.

Beyond this intersection ($m_{F150W2} > 20$ or $m_{F322W2} > 19.5$), the two main groups of stars remain distinguishable down to their respective terminations (see Figs. 2, 3 and 4). The rMS seems to terminate at $m_{F150W2} \sim 24.75$ ($m_{F322W2} \sim 24$), while the bMS ends ~ 0.5 magnitude brighter ($m_{F150W2} \sim 24.25$ or $m_{F322W2} \sim 23.5$). To determine whether these terminations are real and not influenced by completeness effects, we conducted AS tests to assess the completeness of our catalogue, which will be discussed in the next section.

The scatter in photometric colour is driven by the presence of mPOPs, and it encodes the chemical spread in ω Cen. In order to interpret this information, we compared the observed CMD to theoretical isochrones. At this stage, we restricted our analysis to the overall range of $m_{F150W2} - m_{F322W2}$ colour in the CMD as a function of magnitude, and ignored all finer details of the underlying colour distribution. A likelihood-based analysis of star densities in the colour-magnitude space is deferred to a dedicated future study.

At each magnitude, we defined the observed colour range as the interval between the bluest and reddest colour, for which the star density in the colour-magnitude space exceeds a certain threshold that was adjusted by hand to capture the bulk of the colour distribution and exclude outliers. The calculated range is highlighted with yellow shading in panel (a) of Fig. 6. As the basis of our comparison, we adopted two isochrones from Gerasimov et al. (2022) that the authors refer to as 'nominal' (NOM) and 'High Metal High Alpha' (HMHA). Both isochrones were calculated for the helium-enriched sub-population of the cluster with Y = 0.4 (King et al. 2012) that was first recognised in Bedin et al. (2004). The NOM isochrone uses the modal light element (C, N and O) abundances and metallicity ([Fe/H] = −1.7) from the spectroscopic observations of giant members in Marino et al. (2012). The HMHA isochrone was derived from NOM, but with metallicity and α-enhancement (including O) tuned to match the ridgelines of the NIR and optical CMDs from HST photometry. In particular, the HMHA model adopts [M/H] = −1.4, [α/M] = +0.6, as detailed in

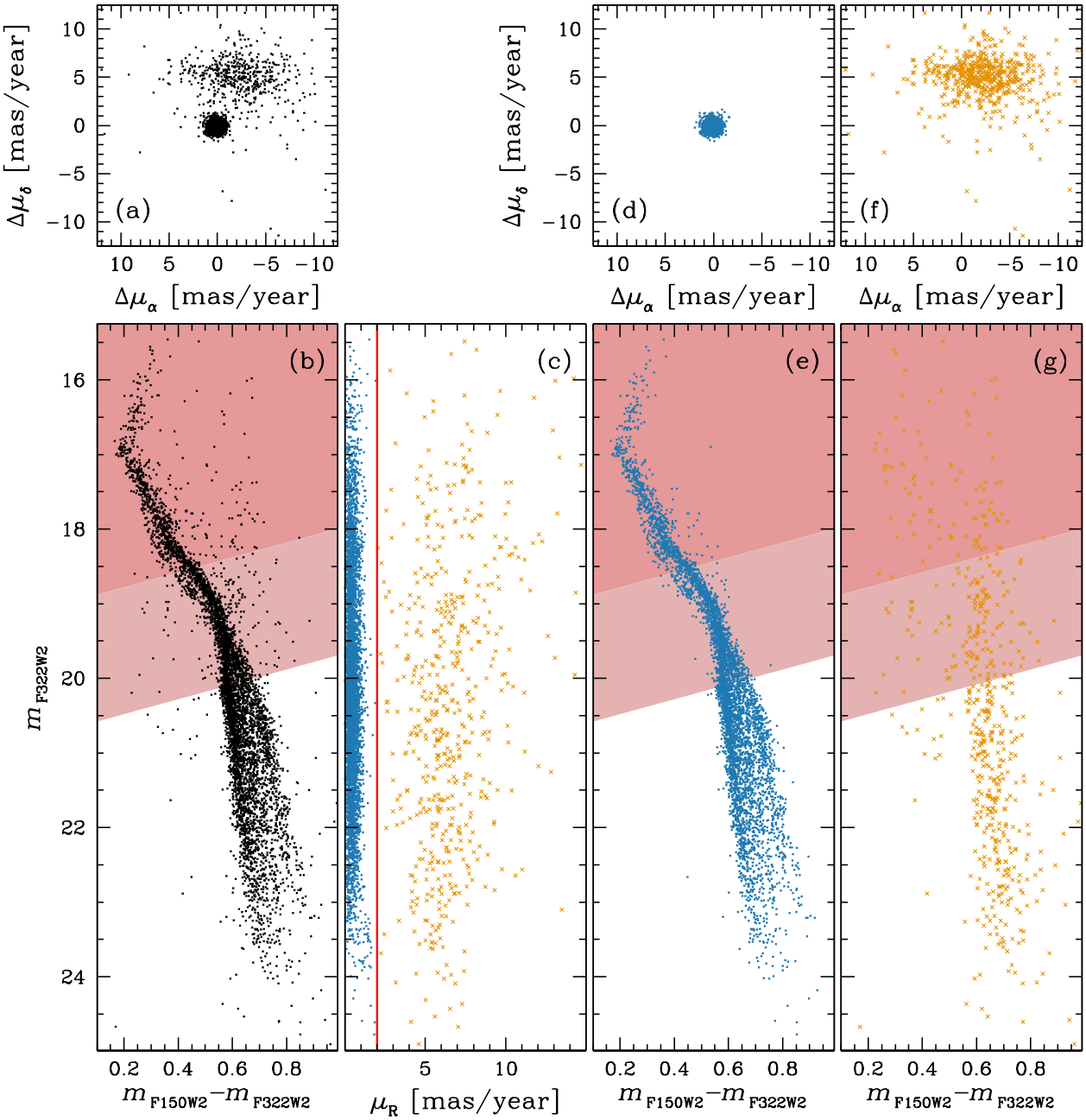

Fig. 4. Cluster membership selection based on PMs, for stars that passed the photometric quality selections and have measurable PMs. (a)–(b) VPD and m_{F322W2} versus $m_{F150W2} - m_{F322W2}$ CMD, respectively. (c) m_{F322W2} magnitude versus the one-dimensional PM (μ_R). The red line separates cluster members from field stars. (d)–(e) VPD and m_{F322W2} versus $m_{F150W2} - m_{F322W2}$ CMD for stars that passed the PM selection. (f)–(g) same diagrams for stars that did not pass the PM selection. In panels (c) through (g), sources that passed the PM selection are represented by blue dots, while those that did not pass are depicted as orange crosses. In panels (b), (e) and (g), the shaded light red and dark red regions highlight areas of the CMDs affected by mild and severe saturation, respectively.

Gerasimov et al. (2022). The overall range of [O/H] covered by these two isochrones spans 1 dex, and overlaps with ∼80% of the spectroscopically inferred distribution[4].

In order to explore the full range of helium mass fraction in ω Cen, we calculated alternative sets of evolutionary models for both NOM and HMHA with Y = 0.25 using the MESA code (Paxton et al. 2011, 2013, 2015, 2018, 2019), and following the method from Gerasimov et al. (2024). We note that the modified versions of the isochrones retain the original atmosphere models with Y = 0.4. Therefore, they have inconsistent helium mass fractions between stellar atmospheres and interiors. We anticipate the error due to this inconsistency to be insignificant since the shape of the lower MS is insensitive to Y (Libralato et al. 2024), and the effect of Y on the upper MS largely originates in the stellar interiors rather than atmospheres (Salaris & Cassisi 2005). We transformed the isochrones to the observed plane using the same parameters and procedure as in Gerasimov et al. (2022), but with a lower interstellar reddening ($E(B-V) = 0.12$,

[4] The [O/H] = [O/M] + [M/H] abundance ratios adopted in NOM and HMHA isochrones are −1.8 and −0.8, respectively (Tables 1 and 2 of Gerasimov et al. 2022). These values correspond to the ∼12th and ∼92nd percentiles of the spectroscopic distribution of [O/H] (upper right panel of Fig. 3 of Marino et al. 2012).

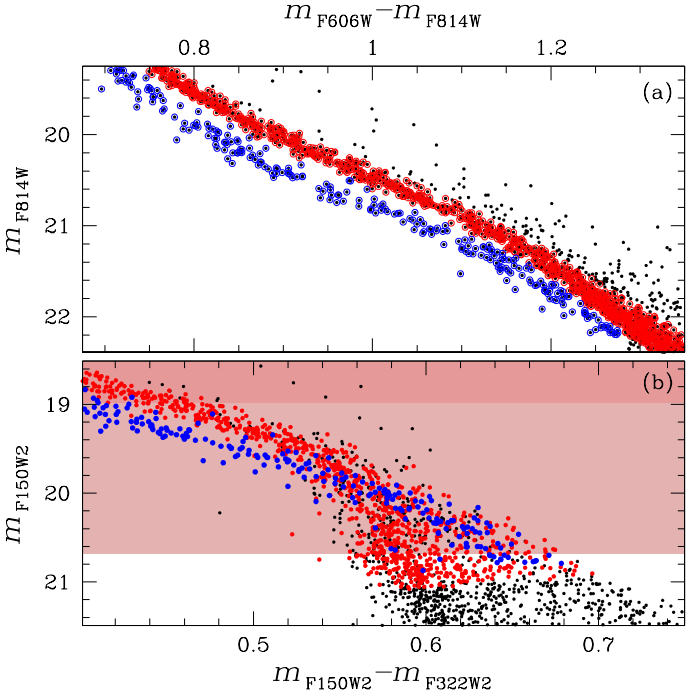

Fig. 5. Crossing of the bMS and rMS stars in the JWST photometry-based CMD. (a) In the HST m_{F814W} versus $m_{F606W} - m_{F814W}$ CMD, we isolated a sample of bMS (black points within blue circles) and rMS (black points within red circles) stars; the two sequences are clearly distinguishable. (b) The same samples highlighted in the JWST m_{F150W2} versus $m_{F150W2} - m_{F322W2}$ CMD, using the same colour code. The shaded light red and dark red regions highlight areas of the CMDs affected by mild and severe saturation, respectively.

which is more consistent with other measurements in the literature, Harris 1996; Calamida et al. 2005) and a more up-to-date reddening law from Gordon et al. (2023).

All four model isochrones (the original and modified versions of NOM and HMHA) are compared to the observed colour spread in panel (b) of Fig. 6. The isochrones are also provided in Tables B.1, B.2, B.3, and B.4 in Appendix B. Both the isochrones and the observed CMD display a clear change of slope near $m_{F322W2} \approx 19.5$. This feature is known as the MS knee (Bono et al. 2010; Saracino et al. 2018), and it is caused by the reduction in the adiabatic gradient due to dissociation of molecular hydrogen (Saumon et al. 1995; Cassisi 2011). Above the knee, the effect of atmospheric chemistry on the shape of the isochrone is subtle, since high effective temperatures ($T_{eff} \gtrsim 4500$ K) suppress the abundances of key infrared absorbers such as H_2O. The small residual effect is driven by two primary factors. First, the mean opacity of the atmosphere reduces T_{eff} at higher metallicities and makes the star redder. This effect is captured in the atmosphere-interior coupling scheme adopted in Gerasimov et al. (2022). The second factor is related to the hydrogen anion (H^-) absorption that has a minimum near 1.6 Mm, producing the characteristic 'H$^-$ bump' in the spectrum (John 1988; Sawicki 2002). The bump becomes more pronounced at higher metallicities, making the $m_{F150W2} - m_{F322W2}$ colour of the star bluer.

The $m_{F150W2} - m_{F322W2}$ CMD therefore provides a unique opportunity to investigate stellar interiors, since these two already small colour-metallicity dependencies due to stellar atmospheres suppress one another. For this reason, the colour of stars above the MS knee is predominantly determined by the stellar interior, and not the atmosphere. In particular, the observed colour of the star is expected to be largely determined by the mean molecular weight of the interior, which is most sensitive to the helium mass fraction, Y. Panel (b) of Fig. 6 clearly shows that Y has the dominant impact on the $m_{F150W2} - m_{F322W2}$ colour, despite the NOM and HMHA isochrones having vastly different chemistries in the atmospheres. The scatter in Y of ∼0.15 is required to fully capture the observed width of the CMD above the MS knee.

The scatter in the CMD colour is noticeably wider below the MS knee due to the increasing effect of atmospheric chemistry including, most notably, infrared absorption bands of H_2O that are regulated directly by [O/Fe], and indirectly by [C/Fe] through the carbon-oxygen chemical reaction network of the atmosphere (Madhusudhan 2012). Both [C/Fe] and [O/Fe] are expected to display large member-to-member variations in GCs due to mPOPs. To determine if these variations alone are sufficient to explain the observed CMD below the MS knee, we adopted the $T_{eff} - \log(g)$ and T_{eff}-luminosity relationships from the Y = 0.25 NOM isochrone, and calculated additional model atmospheres for various values of [C/Fe]/[O/Fe] at 3500 K $\leq T_{eff} \leq$ 5000 K in 100 K steps. The new models were calculated using the `BasicATLAS/ATLAS-9/SYNTHE` setup (Larkin et al. 2023; Kurucz 1970, 2005, 2014; Kurucz & Avrett 1981).

The upper temperature limit for the new models was chosen to approximately match the severe saturation limit of our photometry (also shown in Fig. 6 with dark red shading). The lower temperature limit was chosen out of practical considerations, as `ATLAS` atmospheres are expected to become increasingly unreliable at $T_{eff} \lesssim 3500$ K (Plez 2011). Due to the low metallicity of ω Cen, the effective temperature of 3500 K corresponds to comparatively low stellar masses, varying between 0.10 $M_\odot$ and 0.15 $M_\odot$ among the four isochrones introduced above. We therefore expect the temperature range of new model atmospheres to be sufficiently wide to accommodate nearly all of our data.

For each set of chemical offsets from the composition of the NOM isochrone, we only calculated the updated synthetic spectra, and ignored the effect of altered chemistry on the atmospheric structures, atmosphere-interior coupling and stellar evolution. While these effects are expected to be subdominant on the lower MS, they may not be insignificant. For this reason, this analysis must be considered preliminary and taken with caution.

The synthetic colours and magnitudes of the new models are plotted alongside the NOM Y = 0.25 isochrone in panel (c) of Fig. 6. The figure shows that a spread in [C/Fe]/[O/Fe] alone is sufficient to explain the full width of the observed CMD; however, the red tail of the colour distribution requires a significant fraction of the stars to have simultaneously very low oxygen and very high carbon abundances, which is unlikely due to the strong carbon-oxygen correlation that is expected in GCs in general (see review in Bastian & Lardo 2018), and has been spectroscopically confirmed in ω Cen in particular (Marino et al. 2012).

Alternatively, the red tail of the colour distribution may be due to member-to-member variations in metallicity that have been spectroscopically confirmed in this GC (Marino et al. 2011). Panel (d) of Fig. 6 demonstrates that the red tail of the CMD can be approximated either by models with large but plausible metallicity offsets from NOM, or by more modest metallicity offsets in combination with adjusted light element abundances. The effect of individual metals on the $m_{F150W2} - m_{F322W2}$ colour of the star at $T_{eff} = 4000$ K is shown in Fig. 7. With the exception of oxygen that directly influences infrared absorption features in the spectrum, the most important metal abundances are those of key electron donors (e.g. Mg, Ca, Na) that alter the slope of the stellar continuum.

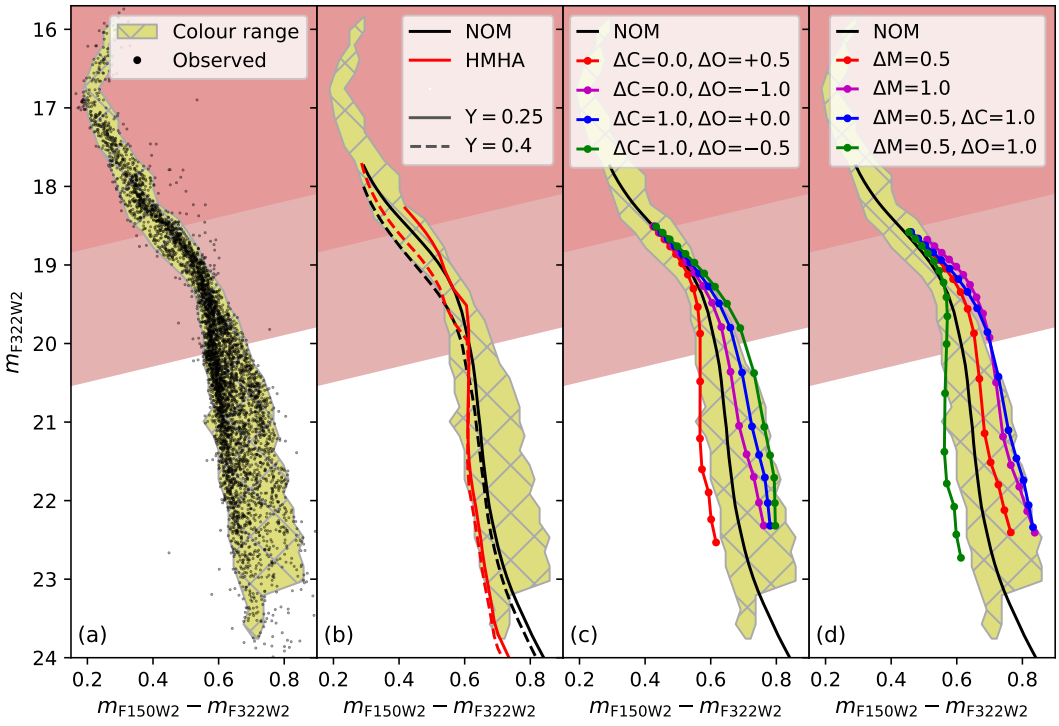

Fig. 6. Comparison between the JWST NIR CMD of ω Cen presented in this study, and model isochrones. For clarity, we do not plot isochrones on the observed CMD directly. Instead, we compare the isochrones to the region of the colour-magnitude space occupied by the cluster, which is shaded in yellow in all panels. Panel (a) demonstrates how this region was chosen in relation to the observed CMD. Panel (b) over-plots two of the isochrones from Gerasimov et al. (2022) with both their original helium mass fraction (Y = 0.4, dashed lines) and with modified evolutionary models that incorporate a near-solar helium abundance (Y = 0.25, solid lines). Panels (c) and (d) show the Y = 0.25 NOM isochrone as well as its lower-MS variations with various chemical offsets. In the legend, ΔC, ΔO and ΔM refers to the offsets in [C/H], [O/H] and [M/H] from the chemical composition adopted for NOM in Gerasimov et al. (2022), where M only refers to metals heavier than oxygen. The shaded light red and dark red regions highlight areas of the CMDs affected by mild and severe saturation, respectively.

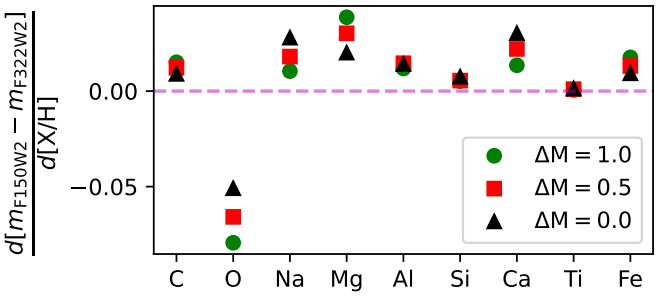

Fig. 7. Effect of offsets in the abundances of selected metals from the chemical composition of the NOM isochrone (panels (b)–(d) of Fig. 6) on the observed $m_{F150W2} - m_{F322W2}$ colour of the star at T_{eff} = 4000 K. The effects are shown at three different metallicity offsets, where M only includes metals heavier than oxygen. Positive values indicate that the star gets redder when the abundance of the element is increased. The 0 (no-effect) horizontal line is shown for reference.

As seen in both panels (c) and (d) of Fig. 6, appropriately chosen isochrones can be used to approximate either tail of the distribution across most of the observed lower MS. We therefore conclude that our observations of ω Cen do not suggest that the chemical spread in the cluster varies with stellar mass.

5. Artificial stars

We used ASs to estimate the completeness of our catalogue for each of the two sequences. We first evaluated the completeness of the JWST data by generating ASs uniformly distributed across the JWST FOV. This allowed us to evaluate the completeness level for the CMD that includes all stars within the JWST field (see Fig. 2). The magnitudes in F322W2 were uniformly distributed within the range $18 < m_{F322W2} < 28.5$, while the corresponding F150W2 magnitudes were assigned based on fiducial lines manually defined in the m_{F322W2} versus $m_{F150W2} - m_{F322W2}$ CMD. One fiducial line was drawn for each of the two sequences, as shown in Fig. 8. We generated 50 000 ASs for each sequence, for a total of 100 000 ASs. The ASs were generated, detected, and measured using KS2, following the same procedures used for the real stars. An AS was considered recovered if the difference between the input and output positions was less than 1 pixel, the difference between the input and output magnitudes was within 0.75 mag (equivalent to ~2.5log2), and it passed the same selection criteria applied to the real stars.

Panel (a) of Fig. 9 shows the injected ASs for the two sequences in the m_{F322W2} versus $m_{F150W2} - m_{F322W2}$ CMD, with injected stars in red and blue, and recovered stars in black. For comparison, panel (b) presents the same CMD for the real stars, with the two fiducial lines overplotted, using the same scale as in panel (a). As clearly visible from panel (a), the recovered ASs exhibit a slight asymmetry in their colour distribution, with redward tails extending from both sequences. This behaviour stems from a known effect of crowding in dense stellar fields. In particular, ASs that fall near bright real stars can be recovered as slightly brighter and redder. This systematic effect produces a characteristic skewness in the colour distribution, manifesting as redward tails.

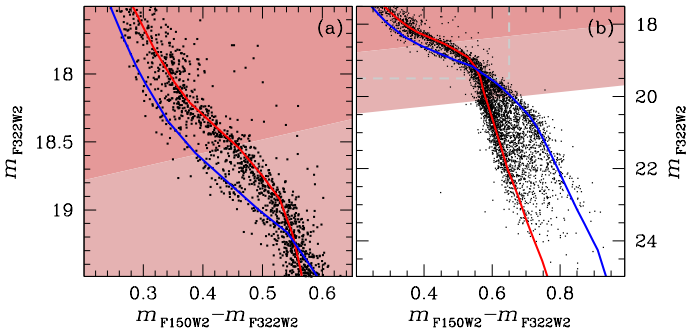

Fig. 8. m_{F322W2} versus $m_{F150W2} - m_{F322W2}$ CMDs of our selected sample of stars, focusing on the upper-MS (panel a) and the entire MS (panel b), with the two fiducials used to generate the ASs. The dashed grey rectangle in panel b highlights the CMD region displayed in panel a. The blue fiducial corresponds to the bMS, while the red fiducial corresponds to the rMS. In the upper part of the MS, the bMS occupies the blue side of the CMD, while the rMS is on the red side. Below the intersection point, the two sequences switch positions. The shaded light red and dark red regions highlight areas of the CMDs affected by mild and severe saturation, respectively.

The completeness, defined as the ratio of recovered stars to the total number of injected stars, is shown as a function of m_{F150W2} and m_{F322W2} magnitudes in panels (b) and (c), for both sequences. In these panels, the completeness for each sequence is represented using the same colour scheme as in panel (a). In this and the other figures of this section, shaded light red and dark red areas qualitatively mark magnitude ranges where MS stars are mildly or severely saturated in at least one filter. Completeness estimates in these magnitude ranges should be interpreted with caution.

From panel (a), it is evident that the recovered ASs extend well beyond the termination points observed in the real stars. The recovered ASs reach the same depth for both sequences, showing no signs of the differing termination magnitudes observed in the real stars. The completeness levels for the two sequences, shown in panels (b) and (c), are nearly identical. At the observed termination magnitudes of the sequences in the real stars ($m_{F322W2} \sim 24$ for the rMS and $m_{F322W2} \sim 23.5$ for the bMS), the completeness remains relatively high, around ∼40%.

These results confirm that the observed terminations in the two sequences are real and not influenced by completeness limitations. The absence of a significant difference in completeness levels between the two sequences further supports the conclusion that the earlier termination of the bMS is an intrinsic feature rather than a consequence of completeness effects.

To evaluate the completeness level for the CMD that includes all stars in the overlapping FOV of both HST and JWST (see Fig. 3), we generated an additional set of 100 000 ASs (50 000 for each sequence), uniformly distributed across the common area. The resulting completeness levels are shown in Fig. 10 as a function of the m_{F150W2} (panel a) and m_{F322W2} (panel b) magnitudes. The completeness values are nearly identical to those obtained when considering the entire JWST field.

To incorporate PM selection into our completeness evaluation and assess the completeness for the stars shown in panel (e) of Fig. 4, we performed the ASs procedure for the HST data as well. We used the same positions and F150W2 and F322W2 magnitudes defined above and determined the corresponding F606W and F814W magnitudes using fiducial lines manually defined in the m_{F322W2} versus $m_{F814W} - m_{F322W2}$ and m_{F322W2} versus $m_{F606W} - m_{F322W}$ CMDs. We ran the ASs stars separately for the JWST and HST datasets and then assessed the displacement of the stars between the two epochs.

Since ASs are generated with identical positions in both epochs, any observed displacement is solely due to spurious offsets caused by noise (e.g. uncertainties in PSF modelling, coordinate transformations, cosmic ray hits, detector cosmetics, etc.), which introduces slight shifts in the recovered positions across epochs. To be considered recovered, an AS must also satisfy the same PM selection criteria applied to real stars, as shown in panel (d) of Fig. 4. By applying this PM selection to ASs, we estimated the fraction of real stars excluded due to these positional offsets, allowing us to incorporate this effect into the overall completeness calculation.

The completeness obtained after applying the PM selection is shown in Fig. 11. As expected, the completeness of both sequences is lower and declines more rapidly towards fainter magnitudes compared to Fig. 10, reaching zero at a brighter magnitude. However, at the termination points of the sequences for real stars ($m_{F322W2} \sim 24$ for the rMS and $m_{F322W2} \sim 23.5$ for the bMS; see panel (d) of Fig. 4), the completeness remains relatively high, around ∼30–40%, confirming the reliability of the sequences termination. Given the consistent completeness between the two sequences, we adopt the completeness values obtained for the rMS in the following analysis.

6. Luminosity and mass function

In this section, we present the LF and MF of ω Cen and its sequences using JWST photometry.

6.1. Combined luminosity and mass functions

We derived the combined (i.e. without matching individual stars to sub-populations) LF and MF of ω Cen by fitting a forward model to the observed m_{F150W2} and m_{F322W2} magnitudes of confirmed members. The likelihood of compatibility between the forward model and a set of photometric measurements with uncertainties, $\{m_i, \sigma_i\}$, is given by the following equation:

$$\mathcal{L} = \prod_i \int_{m_{min}}^{\infty} \phi(m_i)\, \mathrm{comp}(m_i)\, Z(x; m_i, \sigma_i)\, dx, \quad (1)$$

where $\phi(m)$ is the LF (i.e. the likelihood of observing a member with magnitude m), comp(m) is the photometric completeness at magnitude m, and $Z(x; m, \sigma)$ is the probability of measuring magnitude x, given the true magnitude m and the photometric error σ. We took $Z(x; m, \sigma)$ to be a normal distribution with the mean of m and the standard deviation of σ. The brightest considered magnitude, m_{min}, was set to the saturation limit of the instrument, which we conservatively set to $m_{min} = 19$ for both F150W2 and F322W2.

We considered five different families of LF models ($\phi(m)$) listed below:

1. Single population with single-component power-law MF. To construct this model, we used the mass-luminosity relationship (MLR) from only one of the theoretical isochrones shown in panel (b) of Fig. 6. We took the MF to obey a single-component power-law distribution as follows:

$$\xi(M) \propto M^{-\alpha_h}, \quad (2)$$

where $\xi(M)$ is the MF (i.e. the likelihood of observing a member with mass M), and α_h is the slope of the power law.

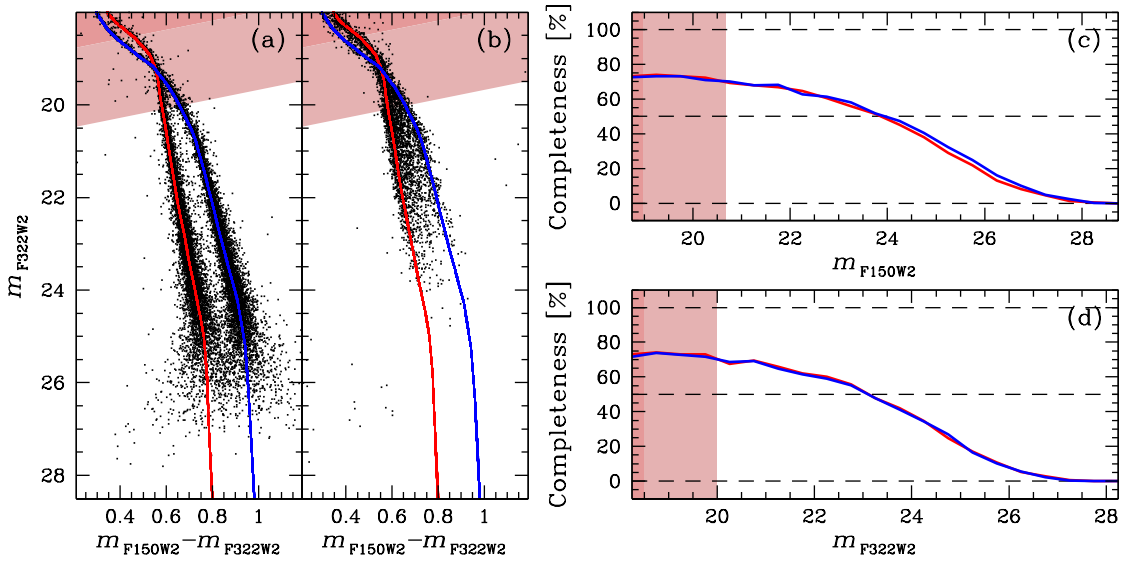

Fig. 9. (a) Injected ASs for the two sequences (blue and red points) in the m_{F150W2} versus $m_{F150W2} - m_{F322W2}$ CMD. Recovered ASs are represented in black. (b) Same as panel (a), but the black points now represent the real stars. (c)–(d) Completeness as a function of the m_{F150W2} and m_{F322W2} magnitude, respectively. The completeness for each sequence is represented using the same colour scheme as in panel (a). Shaded light red and dark red areas qualitatively mark magnitude ranges where MS stars are mildly or severely saturated in at least one filter.

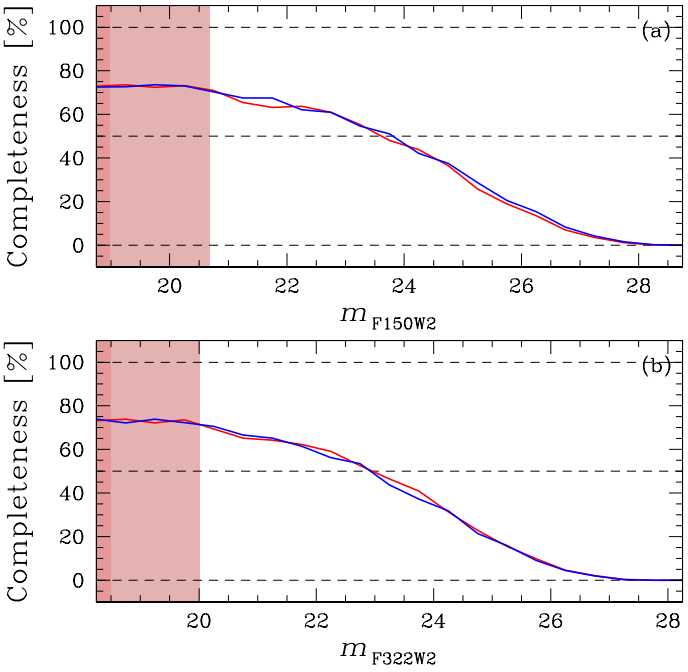

Fig. 10. Completeness as a function of m_{F150W2} (panel a) and m_{F322W2} (panel b) magnitudes for the two sequences in the overlapping region of the HST and JWST fields.

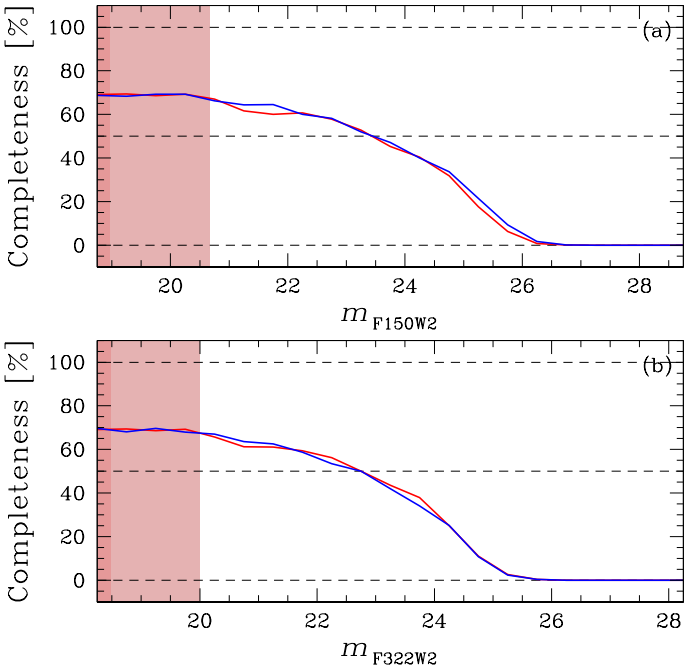

Fig. 11. Same as Fig. 10 but including the PMs selection.

$\xi(M)$ was converted to $\phi(m)$ using the MLR of the adopted isochrone as follows:

$$\phi(m) \propto \xi(M(m)) \left| \frac{dM(m)}{dm} \right|, \tag{3}$$

where $M(m)$ is the MLR, and the derivative was evaluated using a linear spline interpolator.

2. Single population with two-component broken power-law MF. As before, only one isochrone is used to derive the LF, but the MF is allowed to have a break in the power law:

$$\xi(M) \propto \begin{cases} M^{-\alpha_h}, & \text{if } M > M_{pb} \\ M^{-\alpha_l}, & \text{if } M \leq M_{pb} \end{cases}, \tag{4}$$

where α_h and α_l are the power law slopes above and below the break, respectively, and M_{pb} is the stellar mass at which the break occurs.

3. Mixture of two populations with identical single-component power-law MFs. This family of models utilises the single-component MF in Eq. (2); however, the LF is composed of two populations with MLRs adopted from two distinct isochrones in panel (b) of Fig. 6. The contributions of the

two populations to $\phi(m)$ are added with weights given by γ and $(1-\gamma)$, where $0 \leq \gamma \leq 1$ is the mixing ratio. Both populations are assumed to have identical MFs.
4. Mixture of two populations with identical two-component broken power-law MFs. As before, but the shared MF of the two populations has a power law break (Eq. 4).
5. Mixture of two populations with distinct single-component power-law MFs. These models consider two populations with single-component MFs in Eq. 2; however, the slope of the power law is allowed to vary between the populations. We denote the slope of the MF of population 1 as α_h, and the slope of population 2 as α_2.

We did not consider more complicated LF models (e.g. two-population models with distinct broken power-law MFs or three-population models) to avoid over-fitting the observations; however, three-population configurations and arbitrary functional forms of the MF are explored in Section 6.2, where the observed CMD sequences are analysed separately.

The logarithmic likelihood in Eq. 1 was maximised using the Goodman-Weare (Goodman & Weare 2010) Markov chain Monte Carlo (MCMC) sampling with respect to the free parameters defined above (α_h, α_l, α_2, M_{pb} and γ, as appropriate for each family of LF models). We used 32 walkers and 3000 accepted steps per walker. The first 10% of the accepted steps were discarded as burn-in. For single-population LF models, we ran separate MCMC chains for each of the four isochrones in panel (b) of Fig. 6. For LF models with two populations, we considered every possible pair of isochrones, except the ones where both populations have Y = 0.4, as such configurations are clearly unphysical. Furthermore, we ran separate chains for the LFs in F150W2 and F322W2 bands to verify the internal consistency of our results. The best-fit values of the free parameters were taken as the medians of the corresponding MCMC posteriors. The upper and lower 1-sigma asymmetric errors were taken as half-differences between the median and the 97.7 and 2.3 percentiles. The results are summarised in Table 1.

We note that our model fitting method does not require binning of data, and is free of issues associated with histogram-based approaches (e.g. Sollima et al. 2007b; Bedin et al. 2024b; Gerasimov et al. 2024) such as the dependence of results on the bin size and incorrect bin placements due to photometric errors. However, it is possible to visualise the best-fit model in the histogram form by integrating the completeness-corrected LF ($\phi(m_i)$ comp(m_i) in Eq. (1)) in the chosen magnitude bins. This has been carried out in 15 uniform magnitude bins to produce panels (a) and (b) of Figure 12. These panels show the observed member counts in each bin, as well as the best-fitting (based on the maximum likelihood in the MCMC chain for F150W2) LF models from each of the five families described above. In all cases, the best-fitting models are the ones that use the Y = 0.25 NOM isochrone (for single-population models) or both Y = 0.25 and Y = 0.4 NOM isochrones (for mixed population models). The errors shown in Figure 12 were estimated from the scatter among a large number of synthetic datasets that were generated using the best-fit LF model and the estimated completeness and photometric errors of our observations.

We also derived the goodness-of-fit (GoF) for each model as the average absolute difference between the observed and modelled histogram counts, normalised by the estimated count errors. The GoF of each considered LF model is shown in Table 1. Note that for 15 magnitude bins, assuming Gaussian random errors and no systematic errors, the expected GoF is $\approx 0.80 \pm 0.16$[5]. Models with GoFs significantly higher than this value are likely over-fitted, whereas those with lower values are likely under-fitted.

The key conclusions that can be drawn from Table 1 and Fig. 12 are summarised below:

1. Out of single-population models with unbroken single-component MFs, NOM25 and NOM40 provide the best fits to the data (smallest GoF) in F150W2 and F322W2, respectively. The latter case is clearly unphysical, since the majority of members in the observed field are expected to belong to rMS that has a near-solar Y $\approx$ 0.25. As we argue later in this section, this contradiction most likely arises because ω Cen does have a break in the MF within the observed mass range ($\sim$0.1–0.5 $M_\odot$), and because super-solar values of Y mimic such a break in the LF (higher helium mass fractions create a discontinuity in the MLR near 0.3 $M_\odot$, where stars become fully convective). If we only consider single-population unbroken-MF models with Y = 0.25, then NOM25 provides the best fit in both F150W2 and F322W2. The inferred MF slopes in both bands ($\sim$0.7–0.8) are consistent within uncertainties and are also consistent with similar analyses in the literature (e.g. Sollima et al. 2007b; Gerasimov et al. 2022).
2. LF models with broken power-law MFs provide better fits to the data than the unbroken-MF models for all considered configurations. In most cases, adding a break to the MF improves the GoF by a factor of $\sim$2, and brings it in line with the expected value of $\approx 0.80 \pm 0.16$ for a well-fitting model. Out of single-population broken-MF models, NOM25 offers the best fit in both F150W2 and F322W2. In both bands, a power law break around $M_{pb} \approx 0.2\,M_\odot$ is observed with a steep bottom-heavy MF above the break ($\alpha_h > 1$ at $M > M_{pb}$) and a nearly flat MF below the break ($\alpha_l < 0.2$ at $M \leq M_{pb}$). Panel (c) of Fig. 12 shows a histogram of the completeness-corrected inferred stellar masses using the NOM25 broken-MF model. The break in the power law is clearly seen.
3. As is emphasised above, the apparent break in the MF may actually be the result of a discontinuity in the MLR due to the transition from partially to fully convective stellar interiors. In our models, this transition occurs near 0.32 $M_\odot$ for Y = 0.25, and 0.27 $M_\odot$ for Y = 0.4. We however note that the best-fit M_{pb} for the broken-MF NOM25 model was estimated as $0.19 \pm 0.03\,M_\odot$, i.e. over three sigma below the transition. This further corroborates that the observed MF break is likely genuine. On the other hand, all broken-MF single-population models with Y = 0.4 place the break near 0.3 $M_\odot$. For these models, the inferred break is an artefact caused by the discontinuity in the MLR due to the transition from partially to fully convective stellar interiors.
4. While introducing a break in the MF improves the GoF considerably, adding a second population to the mixture has a very small effect. This is apparent in panels (a) and (b) of Fig. 12, where the broken LF models with single and mixed populations are nearly indistinguishable from each other.
5. The best-fitting mixed population models are the combinations of NOM25+NOM40 and NOM25+HMHA25 populations with a common two-component broken MF. In the former case, the mixing ratio was estimated as 0.7 $\pm$ 0.1, suggesting that approximately 20–40% of cluster members are expected to be significantly helium-enriched (bMS).

[5] Estimated as $\int |x|\,Z(x)dx \pm \sqrt{\int x^2 Z(x)dx - \left[\int |x|\,Z(x)dx\right]^2} / \sqrt{15}$, where $Z(x)$ is the standard normal distribution.

Table 1. Best-fit parameters of the LF models.

Band	Population 1	Population 2	α_h	α_l	$M_{pb}/M_\odot$	α_2	γ	GoF
Single population with single-component power-law MF								
F150W2	NOM25	N/A	$0.77^{+0.03}_{-0.03}$	N/A	N/A	N/A	N/A	1.66
	NOM40	N/A	$0.53^{+0.03}_{-0.03}$	N/A	N/A	N/A	N/A	1.84
	HMHA25	N/A	$0.57^{+0.03}_{-0.03}$	N/A	N/A	N/A	N/A	1.90
	HMHA40	N/A	$0.37^{+0.03}_{-0.03}$	N/A	N/A	N/A	N/A	2.56
F322W2	NOM25	N/A	$0.72^{+0.03}_{-0.03}$	N/A	N/A	N/A	N/A	2.03
	NOM40	N/A	$0.46^{+0.03}_{-0.03}$	N/A	N/A	N/A	N/A	1.93
	HMHA25	N/A	$0.46^{+0.03}_{-0.03}$	N/A	N/A	N/A	N/A	2.21
	HMHA40	N/A	$0.21^{+0.04}_{-0.04}$	N/A	N/A	N/A	N/A	2.17
Single population with two-component broken power-law MF								
F150W2	NOM25	N/A	$1.05^{+0.09}_{-0.07}$	$0.13^{+0.15}_{-0.22}$	$0.19^{+0.03}_{-0.02}$	N/A	N/A	0.69
	NOM40	N/A	$1.64^{+0.33}_{-0.25}$	$0.34^{+0.05}_{-0.05}$	$0.31^{+0.02}_{-0.02}$	N/A	N/A	1.09
	HMHA25	N/A	$0.94^{+0.11}_{-0.10}$	$-0.06^{+0.13}_{-0.41}$	$0.21^{+0.03}_{-0.03}$	N/A	N/A	0.90
	HMHA40	N/A	$2.25^{+0.35}_{-0.29}$	$0.08^{+0.05}_{-0.05}$	$0.32^{+0.01}_{-0.01}$	N/A	N/A	1.10
F322W2	NOM25	N/A	$1.20^{+0.13}_{-0.12}$	$0.17^{+0.11}_{-0.27}$	$0.21^{+0.02}_{-0.03}$	N/A	N/A	0.84
	NOM40	N/A	$2.35^{+0.81}_{-0.48}$	$0.29^{+0.05}_{-0.06}$	$0.32^{+0.01}_{-0.02}$	N/A	N/A	1.29
	HMHA25	N/A	$1.17^{+0.13}_{-0.17}$	$-0.04^{+0.08}_{-0.18}$	$0.25^{+0.01}_{-0.03}$	N/A	N/A	0.88
	HMHA40	N/A	$1.85^{+0.37}_{-0.27}$	$-0.07^{+0.05}_{-0.06}$	$0.29^{+0.01}_{-0.01}$	N/A	N/A	1.34
Mixture of two populations with identical single-component power-law MFs								
F150W2	NOM25	NOM40	$0.69^{+0.04}_{-0.04}$	N/A	N/A	N/A	$0.68^{+0.13}_{-0.14}$	1.61
	NOM25	HMHA25	$0.74^{+0.03}_{-0.04}$	N/A	N/A	N/A	$0.89^{+0.05}_{-0.15}$	1.68
	NOM25	HMHA40	$0.74^{+0.03}_{-0.04}$	N/A	N/A	N/A	$0.94^{+0.03}_{-0.08}$	1.68
	HMHA25	NOM40	$0.55^{+0.03}_{-0.03}$	N/A	N/A	N/A	$0.41^{+0.15}_{-0.13}$	1.81
	HMHA25	HMHA40	$0.55^{+0.03}_{-0.04}$	N/A	N/A	N/A	$0.88^{+0.06}_{-0.11}$	1.92
F322W2	NOM25	NOM40	$0.64^{+0.05}_{-0.05}$	N/A	N/A	N/A	$0.66^{+0.14}_{-0.14}$	1.91
	NOM25	HMHA25	$0.70^{+0.04}_{-0.05}$	N/A	N/A	N/A	$0.92^{+0.04}_{-0.13}$	2.03
	NOM25	HMHA40	$0.68^{+0.04}_{-0.06}$	N/A	N/A	N/A	$0.93^{+0.03}_{-0.11}$	2.01
	HMHA25	NOM40	$0.46^{+0.03}_{-0.04}$	N/A	N/A	N/A	$0.38^{+0.13}_{-0.12}$	1.97
	HMHA25	HMHA40	$0.36^{+0.05}_{-0.05}$	N/A	N/A	N/A	$0.55^{+0.15}_{-0.13}$	2.17
Mixture of two populations with identical two-component broken power-law MFs								
F150W2	NOM25	NOM40	$0.98^{+0.10}_{-0.08}$	$0.03^{+0.18}_{-0.36}$	$0.17^{+0.03}_{-0.02}$	N/A	$0.72^{+0.12}_{-0.13}$	0.66
	NOM25	HMHA25	$1.02^{+0.09}_{-0.08}$	$0.05^{+0.15}_{-0.28}$	$0.19^{+0.03}_{-0.02}$	N/A	$0.68^{+0.14}_{-0.18}$	0.66
	NOM25	HMHA40	$1.03^{+0.11}_{-0.09}$	$0.09^{+0.14}_{-0.31}$	$0.19^{+0.03}_{-0.03}$	N/A	$0.80^{+0.09}_{-0.11}$	0.71
	HMHA25	NOM40	$0.83^{+0.17}_{-0.07}$	$-0.36^{+0.30}_{-0.50}$	$0.16^{+0.05}_{-0.02}$	N/A	$0.67^{+0.14}_{-0.16}$	0.89
	HMHA25	HMHA40	$0.96^{+0.23}_{-0.13}$	$-0.03^{+0.12}_{-0.46}$	$0.22^{+0.04}_{-0.04}$	N/A	$0.83^{+0.08}_{-0.17}$	0.99
F322W2	NOM25	NOM40	$1.12^{+0.16}_{-0.15}$	$0.12^{+0.12}_{-0.41}$	$0.20^{+0.02}_{-0.03}$	N/A	$0.81^{+0.09}_{-0.14}$	0.80
	NOM25	HMHA25	$1.19^{+0.13}_{-0.14}$	$0.07^{+0.12}_{-0.25}$	$0.22^{+0.02}_{-0.03}$	N/A	$0.69^{+0.14}_{-0.18}$	0.82
	NOM25	HMHA40	$1.20^{+0.14}_{-0.18}$	$0.11^{+0.11}_{-0.39}$	$0.23^{+0.02}_{-0.04}$	N/A	$0.81^{+0.09}_{-0.13}$	0.87
	HMHA25	NOM40	$0.98^{+0.25}_{-0.17}$	$-0.14^{+0.15}_{-0.69}$	$0.22^{+0.03}_{-0.05}$	N/A	$0.71^{+0.13}_{-0.16}$	1.06
	HMHA25	HMHA40	$1.21^{+0.26}_{-0.29}$	$-0.05^{+0.08}_{-0.54}$	$0.26^{+0.02}_{-0.06}$	N/A	$0.69^{+0.13}_{-0.16}$	0.99
Mixture of two populations with distinct single-component power-law MFs								
F150W2	NOM25	NOM40	$0.79^{+0.08}_{-0.07}$	N/A	N/A	$0.42^{+0.18}_{-2.50}$	$0.59^{+0.19}_{-0.15}$	1.61
	NOM25	HMHA25	$0.78^{+0.04}_{-0.03}$	N/A	N/A	$-2.55^{+1.67}_{-1.19}$	$0.87^{+0.06}_{-0.19}$	1.69
	NOM25	HMHA40	$0.78^{+0.04}_{-0.03}$	N/A	N/A	$-2.08^{+1.32}_{-1.41}$	$0.78^{+0.10}_{-0.21}$	1.66
	HMHA25	NOM40	$0.54^{+0.12}_{-2.05}$	N/A	N/A	$0.55^{+0.09}_{-0.10}$	$0.41^{+0.16}_{-0.18}$	1.81
	HMHA25	HMHA40	$0.58^{+0.04}_{-0.03}$	N/A	N/A	$-2.90^{+1.75}_{-1.02}$	$0.85^{+0.07}_{-0.22}$	1.98
F322W2	NOM25	NOM40	$0.76^{+0.09}_{-0.08}$	N/A	N/A	$0.35^{+0.16}_{-2.06}$	$0.52^{+0.21}_{-0.14}$	1.83
	NOM25	HMHA25	$0.73^{+0.05}_{-0.04}$	N/A	N/A	$-2.57^{+1.60}_{-1.18}$	$0.85^{+0.07}_{-0.22}$	2.05
	NOM25	HMHA40	$0.75^{+0.07}_{-0.05}$	N/A	N/A	$-0.11^{+0.26}_{-2.34}$	$0.60^{+0.19}_{-0.17}$	2.00
	HMHA25	NOM40	$0.43^{+0.13}_{-0.19}$	N/A	N/A	$0.48^{+0.09}_{-0.10}$	$0.38^{+0.15}_{-0.14}$	1.95
	HMHA25	HMHA40	$0.50^{+0.09}_{-0.09}$	N/A	N/A	$0.15^{+0.12}_{-0.16}$	$0.44^{+0.17}_{-0.12}$	2.11

Notes. Population 1 and 2 refer to the isochrones in panel (b) of Fig. 6, whose MLR have been used. '25' and '40' at the end of the population name refer to the Y = 0.25 and Y = 0.4 variants of the isochrones. GoF is the goodness-of-fit as defined in the text. Smaller GoF values imply better fits. See Section 6.1 for the definition of the parameters.

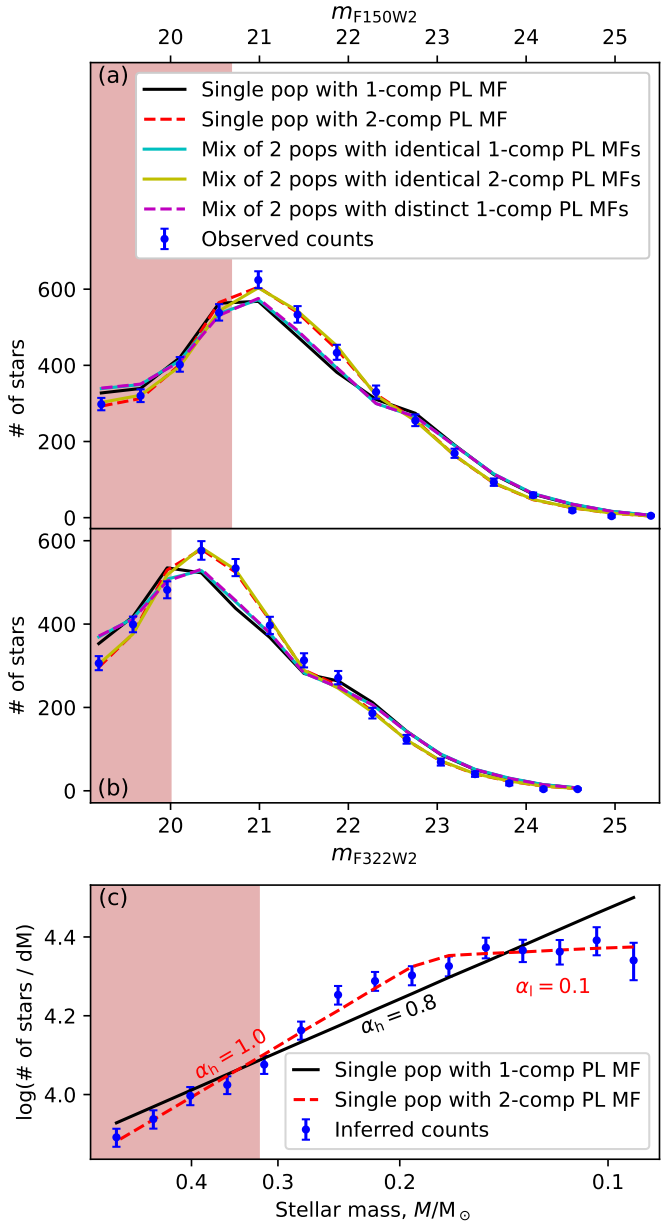

Fig. 12. Observed LFs and derived MF of ω Cen. Panels (a) and (b) show the observed LFs of ω Cen in F150W2 and F322W2 bands, respectively. The LFs are represented as histograms with 15 uniform bins. Over-plotted in both panels are the best-fitting LF models (taken to be the model with the smallest GoF in F150W2) from each of the five families listed in Table 1. The model curves include completeness effects. Panel (c) shows the MF of the cluster based on the inferred stellar masses from the observed F150W2 magnitudes and the Y = 0.25 NOM isochrone, shown in panel (b) of Fig. 6. Unlike panels (a) and (b), the inferred counts in panel (c) have been corrected for photometric completeness. Over-plotted are the best-fitting single-component and two-component power-law MFs. In the legends, *pop* stands for population, *comp* for component, and *PL* for power law. The light red areas qualitatively mark magnitude ranges where MS stars are mildly saturated in at least one filter. The LF and MF values in these regions should be interpreted with caution.

This fraction is consistent with the fraction of observed bMS at this distance from the centre of ω Cen (Scalco et al. 2024a; Bellini et al. 2009). This result is a significant improvement over a similar analysis of HST observations in Gerasimov et al. (2022), where only an upper limit on the population mixing ratio could be derived. In the following sub-section, we verify the calculated mixing ratio by analysing the individual sequences of ω Cen separately.

6. The best-fitting broken-MF models in both single-population and mixed configurations reach the target GoF for a well-fitting model ($\approx$0.80 $\pm$ 0.16). Addition of further degrees of freedom to the model would result in over-fitting. For this reason, we do not consider mixed models with distinct two-component MFs, or mixed models with more than two populations. A far larger sample size is required to explore these more sophisticated models.
7. Allowing a two-population LF model to have distinct MFs in each population has a very small effect on the GoF, compared to the corresponding LF models with identical single-component MFs. For nearly all distinct-MF models, the mixing ratio was found to be consistent with $\gamma = 1$ within 2-sigma bounds, and no reliable constraints on α_2 could be derived. A notable exception is the NOM25+HMHA40 mixture, for which all parameters are well constrained, and the best-fit values are consistent between F150W2 and F322W2. In this model, both populations were found to have similar MF slopes ($\alpha_h \approx \alpha_2 \approx 0.5$), which are comparable to the MF slopes calculated for single-population models with Y = 0.4. It is therefore likely that the best-fit parameters of the NOM25+HMHA40 model are an artefact of the discontinuity in the MLR at the transition between fully and partially convective stellar interiors.

6.2. Luminosity and mass functions for individual stellar populations

In Section 6.1, we analysed the combined LF and MF of ω Cen (where 'combined' refers to the local LF and MF obtained by merging all subpopulations). However, this analysis did not fully exploit all the information available in the CMD, particularly the colour of each star relative to the overall colour distribution, which provides an indication of its likely population membership. As a result, we were limited in our ability to explore more complex models (such as two-population scenarios with distinct broken power-law MFs, or three-population models) and to examine in detail the differences in MF slopes among the individual populations. To overcome these limitations, we adopted a more direct approach, focusing on the LF and MF of the individual stellar populations over a narrower mass range, where the sequences are partially distinguishable. Unlike the method used in Section 6.1, here we adopted a binned approach, as it allows for a more accurate separation of the individual sequences and facilitates a clearer comparison of their respective LFs.

We derived the LFs along the low-MS of the two populations, applying a methodology similar to that outlined in Scalco et al. (2024d). The method is illustrated in Fig. 13. Panel (a) of Fig. 13 shows the m_{F322W2} versus $m_{F150W2} - m_{F322W2}$ CMD for our selected sample of stars, in the magnitude range $20 < m_{F322W2} < 24$, where the separation of the two components is most evident. Note that although completeness remains reliable down to $m_{F322W2} \sim 26$, the statistical limitation of the sample prevents us from classifying or distinguishing additional sequences beyond $m_{F322W2} \sim 24$ (see Figs. 2, 3, 4). We utilised the previously defined fiducials (see Fig. 5) for the two sequences (shown in red and blue in panel (a) of Fig. 13) to verticalise the diagram. For each star, we computed the verticalised colour as

$$\Delta_{F150W2-F322W2} = \frac{X - X_{\text{red fiducial}}}{X_{\text{blue fiducial}} - X_{\text{red fiducial}}}, \quad (5)$$

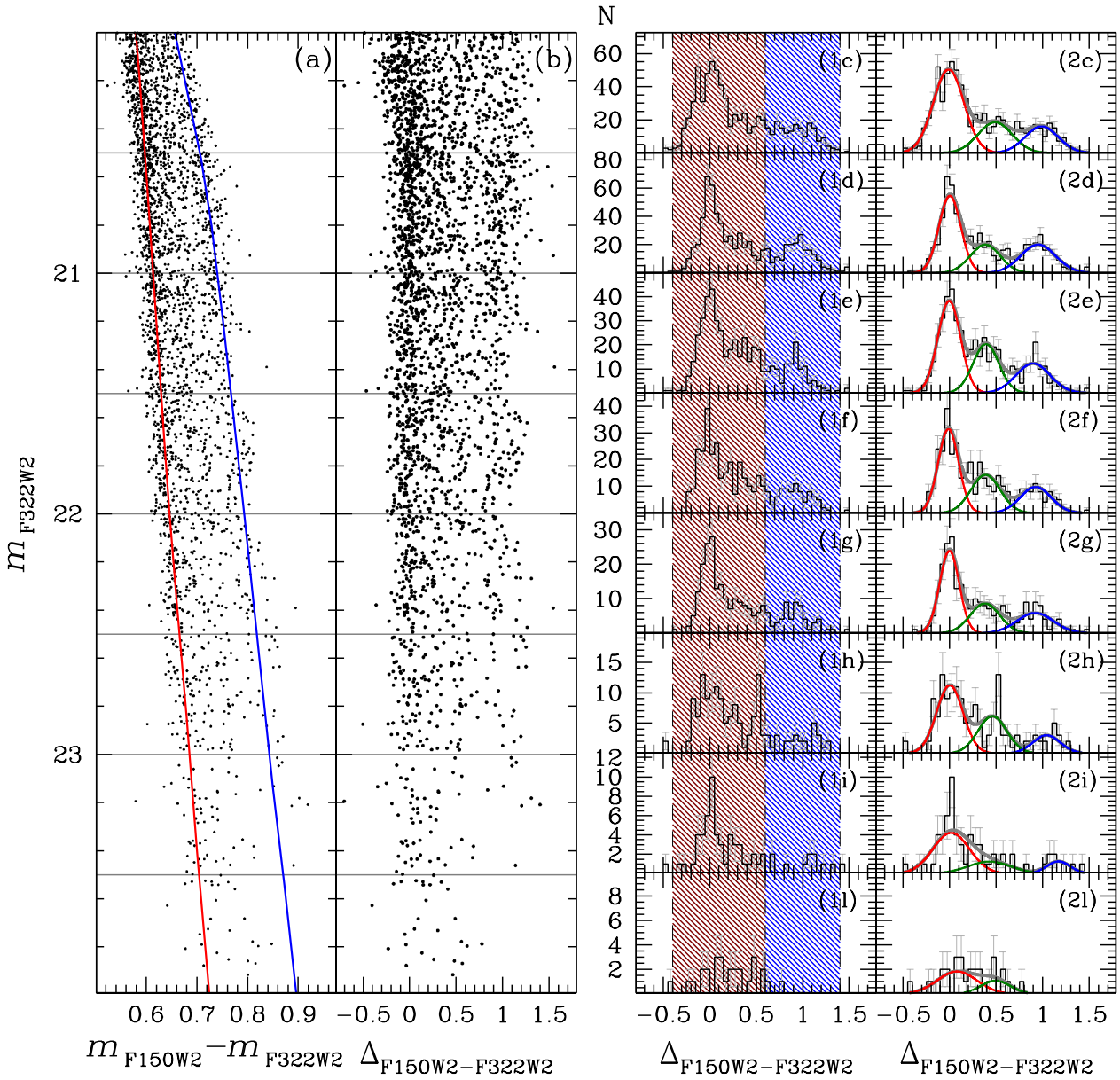

Fig. 13. Procedure for estimating the LFs of the sequences in ω Cen in the low-MS. Panel (a) shows the m_{F322W2} versus $m_{F150W2} - m_{F322W2}$ CMD, focusing on the region where the separation between the components is most evident. The red and blue lines indicate the fiducials of the rMS and bMS, respectively, and are used to construct the verticalised CMD shown in panel (b). Panels (1,2c) through (1,2l) display the histogram distribution of $\Delta_{m_{F150W2}-m_{F322W2}}$ for stars across eight magnitude intervals, as defined by the grey lines in panels (a) and (b). In panels (1c) to (1l), the red and blue regions corresponding to the two sequences are highlighted. These regions are used to estimate the LFs presented in Fig. 14, with values reported in Table 2. Panels (2c) to (2l) present the same histograms with the best-fitting multi-Gaussian models overlaid: three-Gaussian fits in panels (2c) to (2i) and a two-Gaussian fit in panel (2l). The individual Gaussian components are shown in red, green, and blue, while the combined fit is plotted in grey. The obtained LFs are shown in Fig. 15 and the values are reported in Table 3.

where $X = m_{F150W2} - m_{F322W2}$ and $X_{\text{red fiducial}}$, $X_{\text{blue fiducial}}$ are are the colours of the red and blue fiducials, respectively, evaluated at the star's m_{F322W2} magnitude. The resulting verticalised diagram is shown in panel (b) of Fig. 13. We defined 8 magnitude bins in m_{F322W2}, each 0.5 magnitudes wide (indicated by the grey horizontal lines in panels (a) and (b)). The histogram of the verticalised colour for each magnitude bin is shown in panels (1,2c) to (1,2l). We defined two regions: one with $-0.4 < \Delta_{m_{F150W2}-m_{F322W2}} < 0.6$ corresponding to the rMS, and another with $0.6 < \Delta_{m_{F150W2}-m_{F322W2}} < 1.4$ corresponding to the bMS. These regions are represented in panels (1c) to (1l) in red and blue, respectively. For each bin, we counted the number of stars within each of the two defined regions. The resulting values, corrected for completeness, are shown in panel (a) of Fig. 14, using the same colour scheme as in Fig. 13, with error bars representing Poisson errors (this convention for the error bars is adopted throughout this figure and in all subsequent LF and MF plots). As observed, the two LFs exhibit a similar shape, with the rMS containing a larger number of stars in each magnitude interval. The bMS LF declines more rapidly than the rMS LF at fainter magnitudes ($m_{F322W2} > 22.5$) due to the earlier termination of the bMS sequence.

Panel (b) of Fig. 14 presents the population ratio between the two sequences. The error bars represent uncertainties derived through standard error propagation – this approach is also adopted in all subsequent figures displaying population ratios.

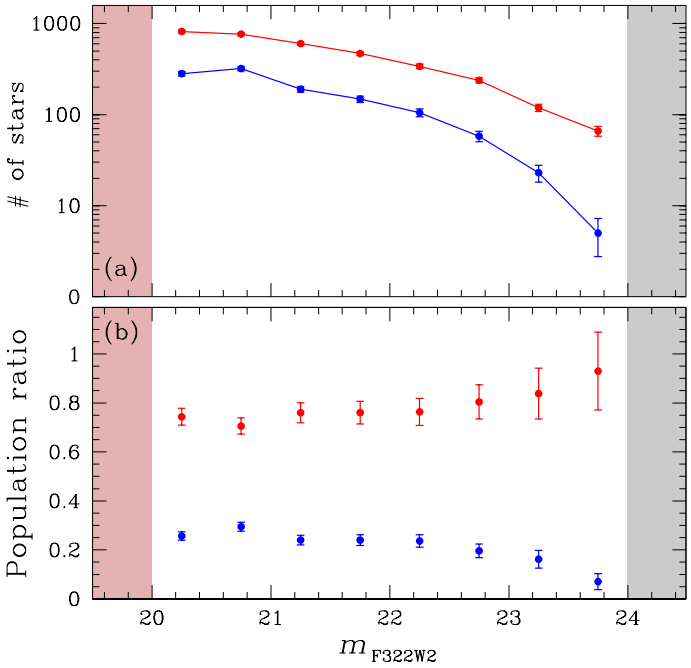

Fig. 14. (a) LF derived using the regions defined in panels (1c) to (1l) of Fig. 13. (b) Population ratio of stars associated with the two sequences. In both panels, the red-shaded region indicates the saturation limit, while the grey-shaded region marks the threshold beyond which the three populations can no longer be distinguished.

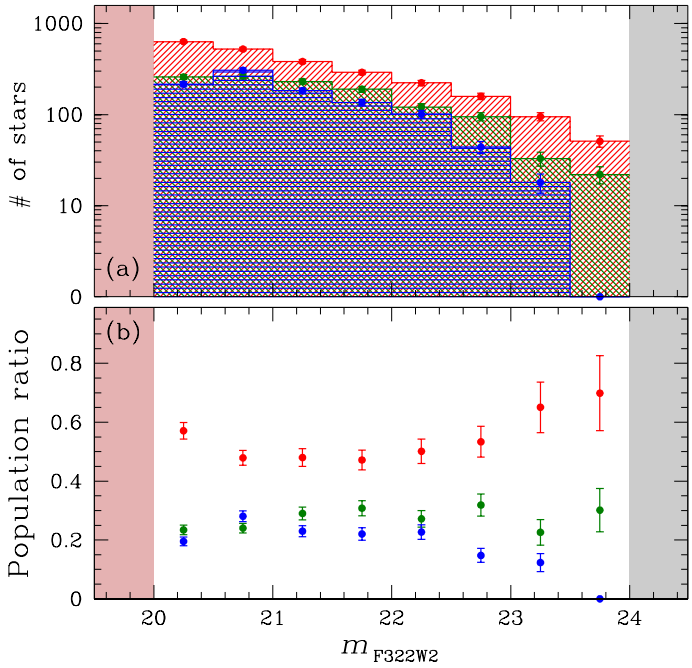

Fig. 15. (a) LF obtained from the three-Gaussian fit shown in panels (2c) to (2l) of Fig. 13, highlighting the drop of the bMS in the final bin ($m_{F150W2} \sim 23.75$). (b) Population ratio of stars associated with the three sequences. As in Fig. 14, both panels feature a red-shaded region indicating the saturation limit and a grey-shaded region marking the threshold beyond which the three populations can no longer be distinguished.

Table 2. Number of stars in the rMS and bMS sequences.

m_{F322W2}	rMS	bMS	rMS/N [%]	bMS/N [%]
20.0–20.5	817 ± 29	282 ± 17	74 ± 3	26 ± 2
20.5–21.0	766 ± 28	320 ± 18	71 ± 3	29 ± 2
21.0–21.5	602 ± 25	190 ± 14	76 ± 4	24 ± 2
21.5–22.0	469 ± 22	148 ± 12	76 ± 5	24 ± 2
22.0–22.5	339 ± 18	105 ± 10	76 ± 6	24 ± 3
22.5–23.0	238 ± 15	58 ± 8	80 ± 7	20 ± 3
23.0–23.5	119 ± 11	23 ± 5	84 ± 10	16 ± 4
23.5–24.0	66 ± 8	5 ± 2	93 ± 16	7 ± 3
	3416 ± 58	1132 ± 34	75 ± 1	25 ± 2

Notes. The values and their relative ratios are obtained using the method illustrated in panels (1c) to (1l) of Fig. 13. The final row reports the total number of stars and the weighted mean of the ratios for the two sequences.

We calculated the weighted mean of the ratios, finding that the rMS accounts for 75% ± 1%, while the bMS accounts for 25% ± 2% of the total number of stars. These values are consistent with those previously reported in literature (Scalco et al. 2024a; Bellini et al. 2009, bMS/rMS ∼ 0.33, for a radial distance corresponding to the field analysed in this study, ∼2−3r_h), and agree with the results discussed in Section 6.1. The data presented in Fig. 14 are listed in Table 2.

To estimate the LFs of the two sequences while accounting for possible contamination between them, we used an alternative method, detailed in Section 4.2 of Scalco et al. (2024d). This method involves determining the number of stars in each bin and in each sequence by fitting the histograms with a multi-Gaussian model, where the number of Gaussians corresponds to the number of sequences. In our case, we initially aimed to fit the histograms with two Gaussian components, one for each sequence. However, upon closer inspection of the verticalised diagram in panel (b) and the histograms in panels (1c, 2c) to (1l, 2l), we observed evidence of a possible third component situated between the two MSs. As discussed in the introduction, ω Cen hosts a highly complex system of mPOPs. While the bMS and rMS constitute the dominant populations, additional stellar groups have been identified, each exhibiting substructures (including the rMS and bMS), resulting in at least 15 distinct populations within ω Cen (Bellini et al. 2017a; Scalco et al. 2024a). The MS presented in panels (a) and (b), and the relative histograms shown in panels (1,2c) to (1,2l), are the result of the contribution of all these stellar populations, which overlap and blend with each other. This complexity necessitates a more precise method to determine the optimal number of Gaussian components to fit.

To address this, we applied a Gaussian mixture model (GMM) to the $\Delta_{m_{F150W2}-m_{F322W2}}$ distribution of stars in each bin, using the expectation-maximisation algorithm from the scikit-learn package (Pedregosa et al. 2011). To find the best model, we calculated the Bayesian Information Criterion (BIC) for models with one to five Gaussian components. A three-Gaussian model provided the lowest BIC for most bins, except for the last two bins (those with, respectively, $23 < m_{F322W2} < 23.5$ and $23.5 < m_{F322W2} < 24$) where a two-Gaussian and a one-Gaussian model were optimal, respectively. In these final bins, the rightmost sequence is barely detectable in the penultimate bin and entirely absent in the last, leaving only the leftmost sequence in the last bin, along with a faint remnant of the middle sequence. Based on these results, we adopted a three-Gaussian model for all bins except the last one, where a two-Gaussian model was used. The GMM fits are shown in grey in panels (2c) to (2l), with

Table 3. Results from the three-Gaussian fit method.

m_{F322W2}	**rMS**	**gMS**	**bMS**	**rMS/N** [%]	**gMS/N** [%]	**bMS/N** [%]	σ_{rMS}	σ_{gMS}	σ_{bMS}	σ^{ART}_{rMS}	σ^{ART}_{bMS}
20.0–20.5	632 ± 25	259 ± 16	216 ± 15	57 ± 3	23 ± 2	20 ± 1	0.16	0.18	0.18	0.02	0.02
20.5–21.0	524 ± 23	263 ± 16	307 ± 18	48 ± 3	24 ± 2	28 ± 2	0.12	0.16	0.19	0.02	0.02
21.0–21.5	382 ± 20	231 ± 15	183 ± 14	48 ± 3	29 ± 2	23 ± 2	0.12	0.14	0.18	0.03	0.03
21.5–22.0	291 ± 17	190 ± 14	136 ± 12	47 ± 3	31 ± 3	22 ± 2	0.11	0.16	0.16	0.03	0.04
22.0–22.5	223 ± 15	121 ± 11	101 ± 10	50 ± 4	27 ± 3	23 ± 3	0.10	0.16	0.19	0.05	0.05
22.5–23.0	159 ± 13	95 ± 10	44 ± 7	53 ± 5	32 ± 4	15 ± 2	0.14	0.15	0.15	0.07	0.07
23.0–23.5	95 ± 10	33 ± 6	18 ± 4	65 ± 9	23 ± 4	12 ± 3	0.20	0.23	0.13	0.08	0.11
23.5–24.0	51 ± 7	22 ± 5	0 ± 0	70 ± 13	30 ± 7	0 ± 0	0.21	0.16	0.00	0.08	0.14
	2357 ± 49	1214 ± 35	1005 ± 32	52 ± 2	26 ± 1	22 ± 2					

Notes. Values are derived using the method illustrated in panels (1c) to (1l) of Fig. 13 for the three sequences. The table also includes the dispersion values (σ) for each Gaussian component for both the real and artificial stars. The final row presents the total number of stars and the weighted average of the ratios for the three sequences.

the individual components represented in red, green, and blue. Hereafter, we refer to the leftmost and rightmost components as the rMS and bMS, respectively, while the middle sequence are referred to as the green MS (gMS).

For each bin, the number of stars in each sequence was estimated from the area under the corresponding Gaussian component. The resulting LFs, corrected for completeness, are illustrated in panel (a) of Fig. 15. As shown, the three LFs follow a similar shape. The rMS is the most populous sequence, the bMS is the least populous, and the gMS lies in between. The only exception occurs at $m_{F322W2} = 20.75$, where a slight peak in the bMS LF temporarily exceeds that of gMS. In the lower part, the LF for the bMS shows a drop, reaching zero in the final bin as the sequence seems to end. Panel (b) shows the population ratios of the three sequences across each magnitude bin. We calculated the weighted mean of the ratios, finding that the rMS accounts for 52% ± 2%, the gMS for 26% ± 1%, and the bMS for 22% ± 2% of the total number of stars. The data presented in Fig. 15 are listed in Table 3.

Table 3 also reports the dispersions (σ) of the three Gaussian components used to model the colour distribution of the MS stars. To assess whether the observed colour spread of the three components arises from intrinsic star-to-star variations in C and O abundances – rather than being solely due to photometric errors – we performed a similar analysis on the ASs shown in panel (a) of Fig. 9. We verticalised the two ASs sequences (black points in panel (a) of Fig. 9) using the same fiducials as for the real stars, and divided the verticalised CMD into 0.5-mag bins in m_{F322W2}, over the same magnitude range used for the real data ($20 < m_{F322W2} < 24$). In each bin, we applied the GMM to estimate the colour dispersion of the two components. The resulting σ values are listed in Table 3. These dispersions are systematically smaller than those measured from the real data, except in the two faintest bins, where photometric errors start to become significant – particularly for the bMS. It is worth noting that the dispersions for the two injected sequences are very similar across the full magnitude range, diverging only in the last two bins. This comparison confirms that the colour dispersion observed in the real stars cannot be explained by photometric errors alone, and is consistent with intrinsic variations in chemical composition, most notably in C and O abundances.

As was pointed out by the referee, the red tail in the artificial stars discussed in Section 5 could, in principle, contribute to the apparent presence of the gMS. However, we note that such red tails involve only a small fraction of the recovered stars, which is insufficient to account for the number of stars observed in the gMS. Moreover, both the colour dispersion and the extent of these tails are significantly smaller than those measured in the real data, particularly in the region occupied by the gMS. We therefore find no indication that the gMS could be the result of this effect.

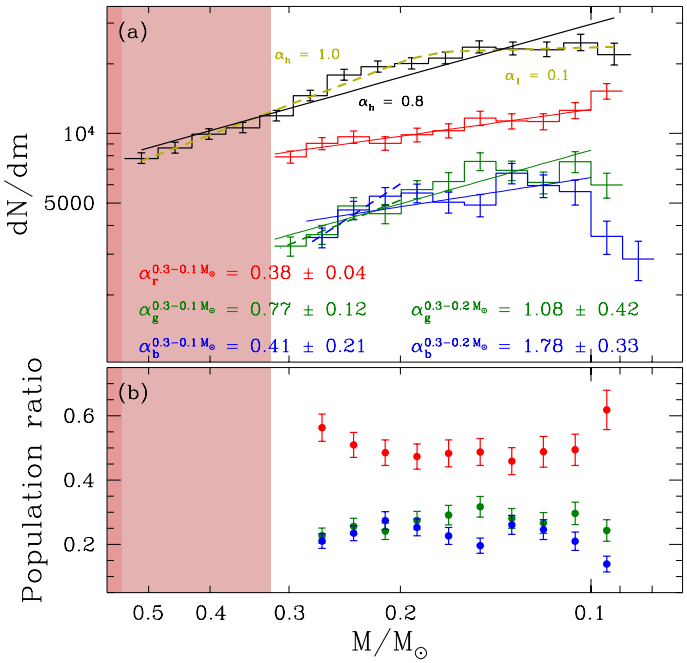

Fig. 16. (a) MFs of the three identified sequences, along with interpolating lines in the mass range $0.1 < M < 0.3\,M_\odot$ (solid lines). The corresponding power-law slopes are indicated in the plot. For the gMS and bMS, we also show fits in the narrower mass range $0.2 < M < 0.3\,M_\odot$ (dashed lines), with their respective slopes also reported. The black histogram represents the combined MF, as shown in panel (c) of Fig. 12. The solid black line and dashed yellow line correspond to the single-component and broken (two-component) power-law fits to the combined MF, respectively, with their slopes provided for reference. (b) Population ratio of stars associated with the three sequences as a function of stellar mass. The shaded light red and dark red regions highlight areas affected by mild and severe saturation, respectively.

To derive the MFs of the three stellar sequences, we adopted a statistical approach. In each magnitude bin defined in Fig. 13,

Table 4. Mass function values for the three sequences.

M/M$_\odot$	rMS	gMS	bMS	rMS/N [%]	gMS/N [%]	bMS/N [%]
0.316–0.282	7909 ± 480	3254 ± 308	–	–	–	–
0.282–0.251	9060 ± 544	3651 ± 345	3546 ± 348	56 ± 4	23 ± 2	21 ± 2
0.251–0.224	9661 ± 595	4858 ± 422	4661 ± 423	51 ± 4	26 ± 2	23 ± 2
0.224–0.199	9057 ± 610	4494 ± 430	5355 ± 480	49 ± 4	24 ± 3	27 ± 3
0.199–0.178	9867 ± 674	5724 ± 514	5521 ± 516	47 ± 4	28 ± 3	25 ± 3
0.178–0.158	10 285 ± 729	6200 ± 566	5047 ± 523	48 ± 4	29 ± 3	23 ± 3
0.158–0.141	11 645 ± 822	7572 ± 663	4903 ± 546	49 ± 4	32 ± 3	19 ± 2
0.141–0.126	11 308 ± 858	6920 ± 671	6728 ± 677	46 ± 4	28 ± 3	26 ± 3
0.126–0.112	11 263 ± 907	6143 ± 670	5943 ± 674	49 ± 5	27 ± 3	24 ± 3
0.112–0.100	12 596 ± 1016	7548 ± 786	5595 ± 693	49 ± 5	30 ± 4	21 ± 3
0.100–0.089	15 237 ± 1184	5986 ± 742	3582 ± 587	62 ± 6	24 ± 3	14 ± 2
0.089–0.076	–	–	2863 ± 556	–	–	–
				50 ± 1	27 ± 1	23 ± 1

Notes. The table also reports the population ratios, as shown in Fig. 16. The final row presents the weighted average of the ratios for the three sequences.

we randomly selected three sub-samples of stars and assigned them to the three populations. The number of stars in each sub-sample was determined according to the area under the corresponding Gaussian component. The magnitudes of the stars were then converted into masses using the isochrones shown in Fig. 6. In particular, we adopted the NOM isochrone with Y = 0.25 for stars assigned to the rMS and gMS, and the NOM isochrone with Y = 0.40 for those assigned to the bMS (see Tables B.1 and B.2 for the corresponding tabulated MLRs). We then computed the MF for each sequence by counting the number of stars in logarithmic mass bins. This entire procedure was repeated 1000 times, and the final MFs were obtained by taking the median number of stars in each mass bin across all realisations.

The resulting MFs for each sequence are shown in Fig. 16, alongside the combined MF previously presented in panel (c) of Fig. 12. The MFs of the individual populations cover a mass range of ∼0.30–0.09 M$_\odot$ for the rMS and gMS, and ∼0.27–0.08 M$_\odot$ for the bMS. Each MF was fitted with a single power-law function (see Eq. (2)) over the mass range 0.1 < M < 0.3 M$_\odot$. The best-fit lines and the corresponding slope values (α) are shown in the figure.

Among the populations, the gMS exhibits the steepest slope ($\alpha_g = 0.77 \pm 0.12$), while the rMS and bMS show similar and flatter slopes ($\alpha_r = 0.38 \pm 0.04$ and $\alpha_b = 0.41 \pm 0.14$, respectively). The MF of the rMS – the most populated sequence – is well characterised by a single power law, indicating a reliable MLR. In contrast, the MFs of the gMS and bMS are noisier and display a noticeable flattening around ∼0.2 M$_\odot$, which also causes the flattening observed in the combined MF at the same mass. This behaviour could indicate a real drop in the number of stars formed below ∼0.2 M$_\odot$, or it might reflect uncertainties in the adopted MLR, particularly at low masses. It is also interesting to notice that for masses smaller than 0.2 M$_\odot$, both the gMS and the bMS are characterised a MF steeper than that of the rMS. This steep slope is responsible for the steepening of the combined MF.

It is important to note that dividing the MS into only three components represents a simplification, given the high level of complexity in the stellar populations of ω Cen. Moreover, the sequence identified as the rMS in the optical HST CMD evolves into a broader colour distribution in the NIR JWST CMD at magnitudes fainter than $m_{F150W2} \simeq 20$ (or $m_{F322W2} \simeq 19$; see Fig. 5), with a main peak corresponding to the red Gaussian component (Fig. 13) and an extended tail that overlaps with the other two components. These features suggest a higher level of complexity in the stellar population structure, and a more refined analysis would require a more sophisticated and detailed approach.

Finally, panel (b) displays the population ratios of the three sequences across each mass bin. We computed the weighted mean of these ratios, finding that the rMS comprises 50% ± 1% of the total number of stars, while the gMS and bMS account for 27% ± 1% and 23% ± 1%, respectively. These values are consistent with those derived from the LFs (see Fig. 15) and listed in Table 3. The data presented in Fig. 16 are listed in Table 4.

Table 5. Hydrogen-burning limits of model isochrones.

Isochrone	HBL [$M_\odot$]	m_{F150W2}	m_{F322W2}
`NOM25`	0.084	27.84	26.19
`NOM40`	0.070	27.81	26.27
`HMHA25`	0.080	28.11	26.37
`HMHA40`	0.066	28.09	26.49

Notes. The table lists the hydrogen-burning limits (HBLs) and the corresponding magnitudes of the model isochrones.

6.3. Note on the effect of the helium mass fraction

As shown in Section 4, the stars of the bMS population are likely helium-enriched compared to their rMS counterparts with the difference in Y between the two populations reaching ∼0.15. In general, a star with enriched helium content has a higher mean molecular weight in the interior, and is more luminous than an equally massive star with a near-solar Y. However, a helium-enriched population of stars would also be able to sustain nuclear fusion at lower stellar masses, thereby lowering the hydrogen-burning limit. These two effects largely suppress each other, making the lower MS almost completely insensitive to Y.

In other words, the observed LF is determined not by the MLR, but by the slope of the MLR with respect to stellar mass (see Eq. (3)). While Y has a large impact on the MLR, its effect

on the slope is subtle compared to the effect of, for example, atmospheric chemistry. For this reason, it is unlikely that the high helium content of the bMS is responsible for its early termination in the CMD compared to the rMS. This is further illustrated in Table 5, where we provide the hydrogen-burning limits and their corresponding magnitudes for the isochrones considered in this study. Note that the large effect of Y on the former does not propagate to the latter.

7. Summary

We presented the first study of the most massive GC in our Galaxy, ω Cen, using recently acquired JWST proprietary data (GO-5110; Bedin et al. 2024a). The results of our investigation are summarised as follows.

We constructed the cluster's NIR CMDs using JWST photometry. Figure A.1 displays these CMDs across broad colour and magnitude ranges, with the onset of mild and strong saturation clearly marked (see Section 2 for further details). In these CMDs, two sequences, – corresponding to the optical bMS and rMS populations of the cluster – can be clearly separated from $m_{\rm F150W2} \sim 18$ ($m_{\rm F322W2} \sim 17.5$) down to $m_{\rm F150W2} \sim 20$ ($m_{\rm F322W2} \sim 19.5$), where they intersect and change their relative positions (see Fig. 5). Below this intersection, the bMS shifts towards redder colours, while the rMS extends over a broad colour range, predominantly favouring bluer colours. The sequences remain distinguishable down to the end of the MS. The sequence corresponding to the bMS stars appears to end – at least – ~0.5 magnitudes brighter than the sequence associated with the rMS population. We performed AS tests to evaluate the completeness of our data and assess whether the observed sequence terminations are intrinsic or driven by incompleteness. The results clearly indicate that the earlier termination of the bMS, which occurs at significantly brighter magnitudes compared to the rMS, is an intrinsic property of the population and not an artefact of completeness effects.

Our comparison with theoretical isochrones confirms that the colour spread in the CMD is primarily driven by variations in helium (Y) abundance above the MS knee and by atmospheric chemistry below the knee. We found that a scatter in Y of approximately 0.15 is necessary to fully capture the observed width of the CMD above the MS knee, reinforcing the idea that helium enhancement plays a dominant role in shaping the stellar populations of ω Cen.

Below the MS knee, the broader colour distribution is largely influenced by variations in oxygen and carbon abundances, which regulate the strength of H_2O absorption bands in the infrared. While the observed spread can be approximated by models with a range of [C/Fe] and [O/Fe], reproducing the full extent of the red tail requires extreme chemical compositions that are unlikely given the known abundance correlations in GCs. Instead, we find that a combination of metallicity variations and light element abundance changes provides a more plausible explanation for the observed CMD morphology.

By combining our JWST data with archival HST observations, as recently presented in Scalco et al. (2024c), we calculated PMs and conducted a membership analysis. We then derived the combined LF and MF of ω Cen, independent of individual populations, by fitting a forward model to the observed magnitudes of confirmed members using an MCMC method. We considered five different families of LF models: (1) a single population with a single-component power-law MF, (2) a single population with a two-component broken power-law MF, (3) a mixture of two populations with identical single-component power-law MFs, (4) a mixture of two populations with identical two-component broken power-law MFs, and (5) a mixture of two populations with distinct single-component power-law MFs. We explored various combinations of isochrones for the populations and evaluated their contributions to the LF.

Our results indicate that the single-population broken power-law models, particularly those using the Y = 0.25 NOM isochrone, provide the best fit. The MF exhibits a break around 0.2 $M_\odot$, with a steep slope above the break and a flatter slope below it. Adding a second population did not substantially improve the fit. The observed LF is predominantly influenced by a single population with an average chemical composition. The mixed population models suggest that approximately 20–40% of cluster members may be helium-enriched.

We then analysed the LF and MF of individual MS populations in ω Cen by focusing on a narrower mass range (~0.3–0.08 $M_\odot$) where the sequences are more clearly separated. The LFs of both sequences exhibit similar shapes, with the rMS containing a larger fraction of stars, accounting for 75% ± 1% of the total population. The bMS LF declines more rapidly than the rMS LF at fainter magnitudes ($m_{\rm F322W2} > 22.5$) due to the earlier termination of the bMS sequence. The bMS-to-rMS number ratio of ~0.33 in this external field agrees with values previously reported by Scalco et al. (2024a), Bellini et al. (2009) for fields at a similar radial distance from the cluster centre.

To refine our LF estimates and account for potential contamination between the sequences, we adopted an alternative approach. We analysed the verticalised CMD by fitting the star distributions in different magnitude bins with a multi-Gaussian model. By closely inspecting the verticalised CMD, we identified evidence of a possible third sequence between the bMS and rMS. To determine the optimal number of Gaussian components for each magnitude bin, we applied a GMM. The GMM results favoured three Gaussian components for most bins. The LFs were then estimated based on the area under each Gaussian component.

The derived LFs show similar shapes for all three components. In the lower part of the LFs, the bMS exhibits a drop, reaching zero in the final bin. The rMS is the most populous, contributing 52% ± 2% of the stars, followed by the gMS at 26% ± 1%, and the bMS at 22% ± 2%.

We then estimated the MF for each of the three sequences in the mass range between 0.3 $M_\odot$ and 0.08 $M_\odot$. The rMS is well-fitted by a single power law in this mass range. The gMS and the bMS, on the other hand, are characterised by a flattening in their MFs for masses <0.2 $M_\odot$ and a slope for masses >0.2 $M_\odot$ that, for both populations, is steeper than that of the rMS. The steepening of the combined MF for masses smaller larger than 0.2 $M_\odot$ and the flattening at masses <0.2 $M_\odot$ are linked to the variation in the MF of the gMS and bMS. The flattening around ~0.2 $M_\odot$ for the gMS and the bMS may reflect a real drop in the number of low-mass stars or might be due to uncertainties in the adopted MLR. The gMS and bMS MF steeper than the rMS for masses >0.2 $M_\odot$ may be the result of the effects of internal two-body relaxation on the radial variation in the MF for the two populations initially more centrally concentrated than the rMS (see Vesperini et al. 2018, for further discussion and details; see also e.g. Livernois et al. 2024 for the effects of two-body relaxation on the evolution towards energy equipartition and Ziliotto et al. (2025), for an observational study of energy equipartition in ω Cen). We emphasise, however, that the narrow mass range and uncertainties in the MF derivation call for caution in the interpretation of the observational results. Additional

studies covering a broader mass range will be necessary to further investigate the differences between the MF of multiple populations in ω Cen.

This work represents the first study of the multiple populations in ω Cen using JWST data. As is well known, ω Cen hosts up to 15 distinct stellar populations in its core. In this study, we focused on the LFs of the sequences identifiable with JWST photometry. However, the complexity of the multiple populations in this cluster requires a more in-depth analysis to fully disentangle and characterise its stellar populations. This is particularly crucial when combining JWST and HST photometry, as demonstrated in a recent study (Scalco et al. 2024b). A comprehensive investigation utilising this combined approach will be the subject of a forthcoming paper (Gerasimov et al., in preparation).

Acknowledgements. Michele Scalco and Luigi Rolly Bedin acknowledge support by MIUR under the PRIN-2017 programme #2017Z2HSMF, by INAF under the PRIN-2019 programme #10-Bedin, and by INAF under the WFAP project, f.o.:1.05.23.05.05. JA, AB, and EV acknowledge support from JWST program GO-5110. We thank our Referee, Dr. Ricardo Salinas, for his prompt and insightful review of our manuscript. His constructive comments and suggestions have significantly improved the clarity and quality of this work. This research is based on observations made with the NASA/ESA Hubble Space Telescope and the NASA/ESA/CSA James Webb Space Telescope. The data were obtained from the Mikulski Archive for Space Telescopes (MAST) at the Space Telescope Science Institute (STScI), which is operated by the Association of Universities for Research in Astronomy, Inc., under NASA contracts NAS 5–26555 for HST and NAS 5-03127 for JWST. These observations are associated with programs HST-GO-14118+14662 and JWST-GO-5110. The data described here may be obtained from http://dx.doi.org/10.17909/7prx-4905.

References

Bastian, N., & Lardo, C. 2018, ARA&A, 56, 83
Bedin, L. R., Piotto, G., Anderson, J., et al. 2004, ApJ, 605, L125
Bedin, L. R., Cassisi, S., Castelli, F., et al. 2005, MNRAS, 357, 1038
Bedin, L. R., King, I. R., Anderson, J., et al. 2008, ApJ, 678, 1279
Bedin, L. R., Salaris, M., Piotto, G., et al. 2009, ApJ, 697, 965
Bedin, L. R., Anderson, J., Apai, D., et al. 2016a, HST Proposal. Cycle 23, ID. #14118
Bedin, L. R., Anderson, J., Apai, D., et al. 2016b, HST Proposal. Cycle 24, ID. #14662
Bedin, L. R., Anderson, J., Apai, D., et al. 2024a, JWST Proposal. Cycle 3, ID. #5110
Bedin, L. R., Nardiello, D., Salaris, M., et al. 2024b, Astron. Nachr., 345, e20240039
Bekki, K., & Freeman, K. C. 2003, MNRAS, 346, L11
Bekki, K., & Norris, J. E. 2006, ApJ, 637, L109
Bellini, A., Piotto, G., Bedin, L. R., et al. 2009, A&A, 507, 1393
Bellini, A., Milone, A. P., Anderson, J., et al. 2017a, ApJ, 844, 164
Bellini, A., Anderson, J., Bedin, L. R., et al. 2017b, ApJ, 842, 6
Bellini, A., Anderson, J., van der Marel, R. P., et al. 2017c, ApJ, 842, 7
Bellini, A., Libralato, M., Bedin, L. R., et al. 2018, ApJ, 853, 86
Bono, G., Stetson, P. B., VandenBerg, D. A., et al. 2010, ApJ, 708, L74
Bushouse, H., Eisenhamer, J., Dencheva, N., et al. 2023, https://doi.org/10.5281/zenodo.6984365
Cadelano, M., Pallanca, C., Dalessandro, E., et al. 2023, A&A, 679, L13
Calamida, A., Stetson, P. B., Bono, G., et al. 2005, ApJ, 634, L69
Cassisi, S. 2011, arXiv e-prints [arXiv:1111.6464]
D'Souza, R., & Rix, H.-W. 2013, MNRAS, 429, 1887
Gaia Collaboration (Prusti, T., et al.) 2016, A&A, 595, A1
Gaia Collaboration (Vallenari, A., et al.) 2023, A&A, 674, A1
Gerasimov, R., Burgasser, A. J., Homeier, D., et al. 2022, ApJ, 930, 24
Gerasimov, R., Bedin, L. R., Burgasser, A. J., et al. 2024, ApJ, 971, 65
Giersz, M., & Heggie, D. C. 2003, MNRAS, 339, 486
Goodman, J., & Weare, J. 2010, Commun. Appl. Math. Comp. Sci., 5, 65
Gordon, K. D., Clayton, G. C., Decleir, M., et al. 2023, ApJ, 950, 86
Gratton, R. G., Carretta, E., & Bragaglia, A. 2012, A&ARv, 20, 50
Gratton, R., Bragaglia, A., Carretta, E., et al. 2019, A&ARv, 27, 8
Griggio, M., Nardiello, D., & Bedin, L. R. 2023, Astron. Nachr., 344, e20230006
Harris, W. E. 1996, AJ, 112, 1487
Harris, W. E. 2010, arXiv e-prints [arXiv:1012.3224]
Ibata, R. A., Bellazzini, M., Malhan, K., Martin, N., & Bianchini, P. 2019, Nat. Astron., 3, 667
John, T. L. 1988, A&A, 193, 189
Johnson, C. I., Pilachowski, C. A., Simmerer, J., & Schwenk, D. 2008, ApJ, 681, 1505
Johnson, C. I., Pilachowski, C. A., Michael Rich, R., & Fulbright, J. P. 2009, ApJ, 698, 2048
Jurcsik, J. 1998, ApJ, 506, L113
King, I. R., Bedin, L. R., Cassisi, S., et al. 2012, AJ, 144, 5
Kurucz, R. L. 1970, SAO Special Report, 309
Kurucz, R. L. 2005, Mem. Soc. Astron. Ital. Suppl., 8, 14
Kurucz, R. L. 2014, Model Atmosphere Codes: ATLAS12 and ATLAS9 (Springer International Publishing), 39
Kurucz, R. L., & Avrett, E. H. 1981, SAO Special Report, 391
Larkin, M. M., Gerasimov, R., & Burgasser, A. J. 2023, AJ, 165, 2
Latour, M., Calamida, A., Husser, T. O., et al. 2021, A&A, 653, L8
Libralato, M., Bellini, A., Bedin, L. R., et al. 2018, ApJ, 854, 45
Libralato, M., Bellini, A., Vesperini, E., et al. 2022, ApJ, 934, 150
Libralato, M., Gerasimov, R., Bedin, L., et al. 2024, A&A, 690, A371
Livernois, A. R., Aros, F. I., Vesperini, E., et al. 2024, MNRAS, 534, 2397
Madhusudhan, N. 2012, ApJ, 758, 36
Marino, A. F., Milone, A. P., Piotto, G., et al. 2011, ApJ, 731, 64
Marino, A. F., Milone, A. P., Piotto, G., et al. 2012, ApJ, 746, 14
Marino, A. F., Milone, A. P., Renzini, A., et al. 2024, ApJ, 969, L8
McLaughlin, D. E., & van der Marel, R. P. 2005, ApJS, 161, 304
Milone, A. P., Piotto, G., Bedin, L. R., et al. 2012, A&A, 540, A16
Milone, A. P., Marino, A. F., Dotter, A., et al. 2023, MNRAS, 522, 2429
Nardiello, D., Libralato, M., Piotto, G., et al. 2018, MNRAS, 481, 3382
Nardiello, D., Bedin, L. R., Burgasser, A., et al. 2022, MNRAS, 517, 484
Nardiello, D., Bedin, L. R., Griggio, M., et al. 2023a, MNRAS, 525, 2585
Nardiello, D., Griggio, M., & Bedin, L. R. 2023b, MNRAS, 521, L39
Norris, J. E. 2004, ApJ, 612, L25
Norris, J. E., & Da Costa, G. S. 1995, ApJ, 447, 680
Norris, J. E., Freeman, K. C., Mayor, M., & Seitzer, P. 1997, ApJ, 487, L187
Pancino, E., Ferraro, F. R., Bellazzini, M., Piotto, G., & Zoccali, M. 2000, ApJ, 534, L83
Paxton, B., Bildsten, L., Dotter, A., et al. 2011, ApJS, 192, 3
Paxton, B., Cantiello, M., Arras, P., et al. 2013, ApJS, 208, 4
Paxton, B., Marchant, P., Schwab, J., et al. 2015, ApJS, 220, 15
Paxton, B., Schwab, J., Bauer, E. B., et al. 2018, ApJS, 234, 34
Paxton, B., Smolec, R., Schwab, J., et al. 2019, ApJS, 243, 10
Pedregosa, F., Varoquaux, G., Gramfort, A., et al. 2011, J. Mach. Learn. Res., 12, 2825
Piotto, G., Villanova, S., Bedin, L. R., et al. 2005, ApJ, 621, 777
Plez, B. 2011, J. Phys.: Conf. Ser., 328, 012005
Rieke, M. J., Kelly, D. M., Misselt, K., et al. 2023, PASP, 135, 028001
Salaris, M., & Cassisi, S. 2005, Evolution of Stars and Stellar Populations (John Wiley and Sons)
Saracino, S., Dalessandro, E., Ferraro, F. R., et al. 2018, ApJ, 860, 95
Sarajedini, A., Bedin, L. R., Chaboyer, B., et al. 2007, AJ, 133, 1658
Saumon, D., Chabrier, G., & van Horn, H. M. 1995, ApJS, 99, 713
Sawicki, M. 2002, AJ, 124, 3050
Scalco, M., Bellini, A., Bedin, L. R., et al. 2021, MNRAS, 505, 3549
Scalco, M., Bedin, L., & Vesperini, E. 2024a, A&A, 688, A180
Scalco, M., Libralato, M., Gerasimov, R., et al. 2024b, A&A, 689, A59
Scalco, M., Salaris, M., Bedin, L. R., et al. 2024c, A&A, 691, A96
Scalco, M., Gerasimov, R., Bedin, L. R., et al. 2024d, Astron. Nachr., 345, e20240018
Scalco, M., Gerasimov, R., Bedin, L. R., et al. 2025, A&A, 694, A68
Smith, V. V., Suntzeff, N. B., Cunha, K., et al. 2000, AJ, 119, 1239
Sollima, A., Ferraro, F. R., Bellazzini, M., et al. 2007a, ApJ, 654, 915
Sollima, A., Ferraro, F. R., & Bellazzini, M. 2007b, MNRAS, 381, 1575
Soltis, J., Casertano, S., & Riess, A. G. 2021, ApJ, 908, L5
Suntzeff, N. B., & Kraft, R. P. 1996, AJ, 111, 1913
Trager, S. C., King, I. R., & Djorgovski, S. 1995, AJ, 109, 218
van de Ven, G., van den Bosch, R. C. E., Verolme, E. K., & de Zeeuw, P. T. 2006, A&A, 445, 513
Vesperini, E., Hong, J., Webb, J. J., D'Antona, F., & D'Ercole, A. 2018, MNRAS, 476, 2731
Wang, S., & Chen, X. 2019, ApJ, 877, 116
Ziliotto, T., Milone, A. P., Cordoni, G., et al. 2025, A&A, submitted [arXiv:2506.21187]

Appendix A: Overview of the JWST photometric catalogue

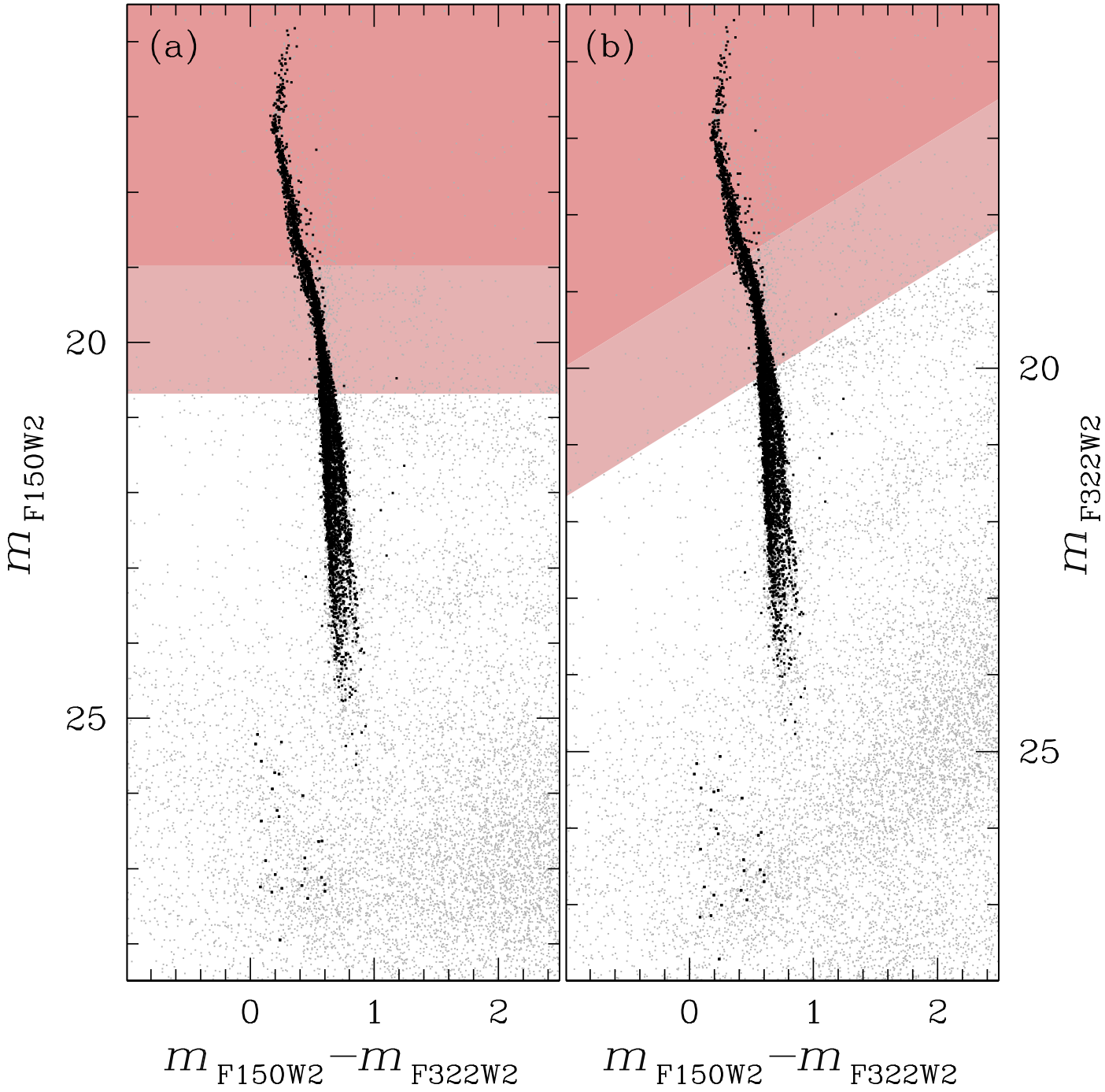

Fig. A.1. Colour-magnitude diagrams of ω Cen using JWST filters. Panel (a) shows the m_{F150W2} versus $m_{\mathrm{F150W2}} - m_{\mathrm{F322W2}}$ CMD, while panel (b) displays the m_{F322W2} versus $m_{\mathrm{F150W2}} - m_{\mathrm{F322W2}}$ CMD, including all stars within the JWST FOV. In both panels, black dots represent stars that pass both the photometric quality and PM selection criteria, while grey dots indicate the remaining stars. The shaded light red and dark red regions highlight areas affected by saturation: the light red region corresponds to saturated photometry, while the dark red region marks severe saturation, where even `frame zero` is saturated.

Appendix B: Mass-luminosity relations

Table B.1. Mass–luminosity relation from the NOM25 model.

$M/M_\odot$	T_{eff} [K]	m_{F150W2}	m_{F322W2}	$m^{reddened}_{F150W2}$	$m^{reddened}_{F322W2}$	$M/M_\odot$	T_{eff} [K]	m_{F150W2}	m_{F322W2}	$m^{reddened}_{F150W2}$	$m^{reddened}_{F322W2}$
0.0835	1326	28.5716	26.6109	28.6539	26.6285	0.1277	3618	22.6685	22.0451	22.7410	22.0663
0.0836	1343	28.5085	26.5738	28.5909	26.5916	0.1372	3674	22.4687	21.8517	22.5412	21.8729
0.0839	1406	28.2747	26.4414	28.3575	26.4592	0.1484	3739	22.2525	21.6417	22.3249	21.6630
0.0839	1428	28.1914	26.3977	28.2745	26.4156	0.1604	3813	22.0333	21.4287	22.1058	21.4501
0.0842	1503	27.9088	26.2544	27.9930	26.2724	0.1729	3874	21.8317	21.2317	21.9042	21.2531
0.0844	1579	27.6186	26.0950	27.7035	26.1132	0.1871	3904	21.6542	21.0575	21.7267	21.0789
0.0844	1609	27.5086	26.0312	27.5937	26.0494	0.2062	3933	21.4502	20.8591	21.5227	20.8806
0.0846	1693	27.2394	25.8559	27.3244	25.8742	0.2284	3961	21.2432	20.6572	21.3157	20.6787
0.0847	1780	26.9732	25.6822	27.0580	25.7007	0.2539	3990	21.0370	20.4557	21.1095	20.4772
0.0849	1864	26.7293	25.5259	26.8141	25.5446	0.2831	4017	20.8320	20.2569	20.9046	20.2784
0.0850	1944	26.5138	25.3814	26.5983	25.4002	0.3170	4047	20.6235	20.0574	20.6961	20.0790
0.0852	2036	26.2801	25.2189	26.3642	25.2378	0.3559	4089	20.3942	19.8395	20.4668	19.8611
0.0854	2108	26.0932	25.0886	26.1770	25.1076	0.3968	4162	20.1166	19.5763	20.1893	19.5979
0.0857	2184	25.9133	24.9337	25.9960	24.9529	0.4309	4258	19.8574	19.3369	19.9303	19.3585
0.0861	2288	25.6578	24.7009	25.7390	24.7205	0.4604	4376	19.6168	19.1223	19.6900	19.1440
0.0864	2357	25.5094	24.5908	25.5903	24.6104	0.4797	4474	19.4566	18.9837	19.5300	19.0053
0.0870	2451	25.3086	24.4470	25.3890	24.4666	0.4853	4506	19.4092	18.9430	19.4827	18.9646
0.0875	2541	25.1170	24.2954	25.1967	24.3151	0.5036	4619	19.2596	18.8168	19.3334	18.8384
0.0881	2622	24.9556	24.1539	25.0344	24.1738	0.5200	4734	19.1294	18.7090	19.2036	18.7307
0.0889	2712	24.7795	23.9945	24.8574	24.0145	0.5350	4845	19.0128	18.6131	19.0873	18.6348
0.0897	2798	24.6034	23.8373	24.6804	23.8575	0.5491	4955	18.9047	18.5244	18.9796	18.5462
0.0907	2882	24.4436	23.6943	24.5199	23.7146	0.5545	4998	18.8643	18.4914	18.9393	18.5131
0.0919	2968	24.2908	23.5560	24.3664	23.5764	0.5677	5107	18.7650	18.4103	18.8403	18.4320
0.0930	3036	24.1605	23.4381	24.2356	23.4586	0.5804	5213	18.6702	18.3326	18.7459	18.3543
0.0946	3116	23.9920	23.2858	24.0665	23.3064	0.5928	5318	18.5765	18.2553	18.6524	18.2770
0.0966	3192	23.8194	23.1285	23.8934	23.1492	0.6052	5422	18.4819	18.1764	18.5581	18.1981
0.0993	3268	23.6395	22.9628	23.7130	22.9837	0.6176	5522	18.3850	18.0942	18.4614	18.1159
0.1028	3344	23.4515	22.7879	23.5247	22.8088	0.6299	5621	18.2853	18.0086	18.3619	18.0304
0.1073	3418	23.2567	22.6049	23.3296	22.6259	0.6425	5720	18.1813	17.9185	18.2582	17.9402
0.1129	3490	23.0610	22.4192	23.1338	22.4403	0.6551	5818	18.0719	17.8223	18.1490	17.8441
0.1196	3556	22.8667	22.2345	22.9393	22.2557	0.6680	5915	17.9547	17.7177	18.0319	17.7395

Notes. The table lists stellar masses, effective temperatures, and magnitudes in the F150W2 and F322W2 filters, both with and without reddening corrections.

Table B.2. Mass–luminosity relation from the NOM40 model.

$M/M_\odot$	T_{eff} [K]	m_{F150W2}	m_{F322W2}	$m^{reddened}_{F150W2}$	$m^{reddened}_{F322W2}$	$M/M_\odot$	T_{eff} [K]	m_{F150W2}	m_{F322W2}	$m^{reddened}_{F150W2}$	$m^{reddened}_{F322W2}$
0.0700	1363	28.6613	26.7627	28.7439	26.7805	0.1172	3704	22.6225	22.0087	22.6950	22.0300
0.0701	1413	28.4807	26.6603	28.5637	26.6782	0.1264	3770	22.4039	21.7959	22.4764	21.8173
0.0702	1485	28.2132	26.5222	28.2971	26.5401	0.1361	3875	22.1658	21.5654	22.2383	21.5868
0.0703	1506	28.1338	26.4814	28.2180	26.4994	0.1452	3908	22.0041	21.4076	22.0766	21.4290
0.0704	1593	27.7885	26.2917	27.8736	26.3098	0.1571	3935	21.8311	21.2401	21.9036	21.2615
0.0705	1688	27.4746	26.0877	27.5597	26.1061	0.1730	3965	21.6324	21.0471	21.7050	21.0686
0.0706	1780	27.1868	25.8976	27.2717	25.9161	0.1917	3996	21.4303	20.8503	21.5029	20.8718
0.0707	1866	26.9316	25.7314	27.0164	25.7501	0.2135	4025	21.2269	20.6543	21.2996	20.6758
0.0708	1949	26.7065	25.5774	26.7911	25.5962	0.2390	4058	21.0188	20.4552	21.0915	20.4767
0.0709	2034	26.4796	25.4172	26.5637	25.4361	0.2681	4099	20.8072	20.2548	20.8798	20.2764
0.0711	2104	26.2911	25.2853	26.3749	25.3043	0.2945	4148	20.5749	20.0319	20.6476	20.0535
0.0712	2168	26.1322	25.1473	26.2151	25.1664	0.3010	4165	20.5163	19.9765	20.5891	19.9981
0.0715	2252	25.9230	24.9583	26.0046	24.9777	0.3264	4253	20.2699	19.7481	20.3428	19.7696
0.0718	2315	25.7724	24.8269	25.8533	24.8464	0.3496	4370	20.0263	19.5300	20.0995	19.5517
0.0723	2400	25.5982	24.7058	25.6789	24.7254	0.3646	4468	19.8634	19.3887	19.9368	19.4103
0.0728	2495	25.3874	24.5513	25.4676	24.5710	0.3694	4502	19.8108	19.3435	19.8843	19.3651
0.0734	2575	25.2273	24.4148	25.3066	24.4346	0.3837	4617	19.6577	19.2141	19.7315	19.2358
0.0742	2668	25.0456	24.2522	25.1239	24.2721	0.3961	4727	19.5268	19.1048	19.6010	19.1265
0.0750	2757	24.8672	24.0921	24.9446	24.1122	0.4073	4833	19.4100	19.0078	19.4845	19.0295
0.0759	2843	24.6986	23.9416	24.7752	23.9618	0.4179	4937	19.3012	18.9175	19.3760	18.9393
0.0769	2931	24.5397	23.7988	24.6156	23.8192	0.4281	5040	19.1968	18.8307	19.2719	18.8524
0.0781	3018	24.3847	23.6586	24.4599	23.6791	0.4381	5141	19.0944	18.7450	19.1698	18.7667
0.0795	3097	24.2219	23.5120	24.2965	23.5326	0.4479	5243	18.9927	18.6596	19.0684	18.6813
0.0800	3122	24.1671	23.4622	24.2415	23.4829	0.4576	5344	18.8915	18.5741	18.9675	18.5958
0.0820	3207	23.9797	23.2917	24.0536	23.3125	0.4671	5444	18.7898	18.4873	18.8660	18.5090
0.0844	3284	23.8016	23.1280	23.8751	23.1488	0.4766	5543	18.6844	18.3965	18.7609	18.4183
0.0875	3361	23.6148	22.9542	23.6880	22.9752	0.4863	5642	18.5741	18.3004	18.6508	18.3221
0.0915	3439	23.4204	22.7714	23.4933	22.7925	0.4960	5740	18.4574	18.1973	18.5343	18.2191
0.0964	3513	23.2235	22.5851	23.2963	22.6062	0.5059	5839	18.3317	18.0849	18.4088	18.1067
0.1023	3582	23.0267	22.3984	23.0993	22.4196	0.5159	5937	18.1935	17.9593	18.2708	17.9811
0.1092	3646	22.8265	22.2064	22.8991	22.2276						

Notes. The table has the same structure and content as Table B.1, but refers to the NOM40 model.

Table B.3. Mass–luminosity relation from the HMHA25 model.

$M/M_\odot$	T_{eff} [K]	m_{F150W2}	m_{F322W2}	$m^{reddened}_{F150W2}$	$m^{reddened}_{F322W2}$	$M/M_\odot$	T_{eff} [K]	m_{F150W2}	m_{F322W2}	$m^{reddened}_{F150W2}$	$m^{reddened}_{F322W2}$
0.0600	876	31.0094	27.9167	31.0943	27.9327	0.0951	2929	23.9720	23.3425	24.0459	23.3628
0.0655	939	30.3506	27.5939	30.4339	27.6101	0.0981	3011	23.7976	23.1743	23.8712	23.1948
0.0700	979	30.2239	27.3969	30.3002	27.4133	0.1017	3086	23.6214	23.0052	23.6948	23.0257
0.0725	1006	30.2140	27.3423	30.2874	27.3589	0.1064	3161	23.4335	22.8249	23.5068	22.8456
0.0739	1040	30.0181	27.2836	30.0934	27.3001	0.1120	3232	23.2440	22.6420	23.3171	22.6627
0.0760	1108	29.5327	27.0911	29.6105	27.1077	0.1188	3299	23.0544	22.4577	23.1274	22.4785
0.0774	1156	29.2349	26.9057	29.3113	26.9225	0.1268	3364	22.8582	22.2688	22.9312	22.2897
0.0779	1177	29.1027	26.8249	29.1785	26.8418	0.1361	3421	22.6637	22.0809	22.7366	22.1018
0.0787	1228	28.8396	26.6662	28.9148	26.6832	0.1472	3491	22.4478	21.8738	22.5206	21.8949
0.0790	1257	28.7180	26.5928	28.7930	26.6099	0.1588	3571	22.2286	21.6621	22.3015	21.6832
0.0796	1321	28.4066	26.4498	28.4833	26.4670	0.1710	3624	22.0395	21.4775	22.1123	21.4987
0.0797	1339	28.2870	26.4202	28.3655	26.4374	0.1858	3657	21.8524	21.2927	21.9252	21.3139
0.0802	1409	27.8620	26.3091	27.9465	26.3264	0.2046	3691	21.6417	21.0839	21.7144	21.1051
0.0805	1470	27.6884	26.1947	27.7727	26.2122	0.2261	3722	21.4322	20.8739	21.5049	20.8951
0.0806	1504	27.5988	26.1352	27.6829	26.1528	0.2506	3753	21.2224	20.6629	21.2951	20.6842
0.0809	1600	27.4362	25.9869	27.5188	26.0047	0.2786	3787	21.0128	20.4520	21.0854	20.4733
0.0811	1689	27.0805	25.8019	27.1641	25.8198	0.3102	3821	20.8053	20.2436	20.8778	20.2649
0.0814	1770	26.7972	25.6054	26.8800	25.6235	0.3463	3857	20.6110	20.0495	20.6835	20.0708
0.0816	1833	26.6014	25.4628	26.6834	25.4809	0.3791	3908	20.3703	19.8092	20.4427	19.8306
0.0819	1911	26.3859	25.3085	26.4673	25.3268	0.3890	3925	20.3020	19.7417	20.3744	19.7632
0.0823	1982	26.2051	25.1914	26.2863	25.2098	0.4230	4002	20.0481	19.4936	20.1205	19.5150
0.0829	2093	25.9101	24.9861	25.9907	25.0046	0.4542	4069	19.7939	19.2798	19.8663	19.3013
0.0834	2181	25.6850	24.8170	25.7647	24.8358	0.4843	4179	19.5313	19.0432	19.6037	19.0648
0.0840	2264	25.4766	24.6566	25.5555	24.6755	0.5046	4277	19.3528	18.8782	19.4252	18.8998
0.0846	2347	25.2796	24.4991	25.3577	24.5181	0.5110	4310	19.2977	18.8282	19.3701	18.8498
0.0855	2432	25.0799	24.3394	25.1572	24.3587	0.5303	4426	19.1354	18.6855	19.2080	18.7072
0.0864	2516	24.8854	24.1833	24.9621	24.2027	0.5469	4535	19.0030	18.5718	19.0759	18.5936
0.0876	2600	24.6962	24.0137	24.7721	24.0334	0.5621	4641	18.8884	18.4754	18.9616	18.4971
0.0889	2683	24.5110	23.8463	24.5864	23.8662	0.5765	4746	18.7846	18.3894	18.8581	18.4111
0.0906	2765	24.3295	23.6824	24.4043	23.7024	0.5902	4849	18.6873	18.3094	18.7613	18.3311
0.0926	2847	24.1502	23.5144	24.2245	23.5346	0.6000	4923	18.6184	18.2526	18.6927	18.2743

Notes. The table has the same structure and content as Table B.1, but refers to the HMHA25 model.

Table B.4. Mass–luminosity relation from the HMHA40 model.

$M/M_\odot$	T_{eff} [K]	m_{F150W2}	m_{F322W2}	$m^{reddened}_{F150W2}$	$m^{reddened}_{F322W2}$	$M/M_\odot$	T_{eff} [K]	m_{F150W2}	m_{F322W2}	$m^{reddened}_{F150W2}$	$m^{reddened}_{F322W2}$
0.0600	991	30.4865	27.6025	30.5609	27.6189	0.0862	3091	23.8141	23.1989	23.8875	23.2194
0.0606	1000	30.5013	27.5873	30.5745	27.6038	0.0902	3170	23.6254	23.0183	23.6987	23.0390
0.0624	1053	30.1610	27.4707	30.2368	27.4873	0.0950	3244	23.4360	22.8356	23.5091	22.8564
0.0638	1114	29.7069	27.2730	29.7844	27.2897	0.1007	3316	23.2446	22.6504	23.3176	22.6713
0.0641	1132	29.5940	27.2027	29.6709	27.2195	0.1074	3379	23.0514	22.4642	23.1244	22.4852
0.0649	1177	29.3136	27.0312	29.3893	27.0481	0.1153	3442	22.8496	22.2698	22.9225	22.2908
0.0652	1197	29.1869	26.9548	29.2622	26.9718	0.1243	3513	22.6326	22.0612	22.7055	22.0822
0.0656	1255	28.9354	26.8050	29.0104	26.8220	0.1338	3618	22.3916	21.8293	22.4644	21.8505
0.0658	1281	28.8239	26.7377	28.8988	26.7548	0.1427	3655	22.2265	21.6670	22.2993	21.6882
0.0661	1345	28.4528	26.6167	28.5319	26.6339	0.1542	3688	22.0459	21.4885	22.1186	21.5097
0.0662	1362	28.3422	26.5901	28.4230	26.6073	0.1693	3721	21.8433	21.2856	21.9160	21.3069
0.0664	1418	28.0347	26.4920	28.1192	26.5094	0.1869	3755	21.6378	21.0787	21.7104	21.0999
0.0666	1470	27.8727	26.3837	27.9570	26.4012	0.2072	3789	21.4319	20.8716	21.5045	20.8929
0.0669	1533	27.7282	26.2735	27.8119	26.2911	0.2304	3822	21.2287	20.6682	21.3013	20.6895
0.0669	1561	27.6830	26.2303	27.7662	26.2480	0.2573	3860	21.0215	20.4610	21.0940	20.4824
0.0671	1646	27.4360	26.0711	27.5190	26.0890	0.2880	3916	20.7549	20.1950	20.8274	20.2165
0.0671	1648	27.4271	26.0665	27.5102	26.0844	0.3154	3993	20.4918	19.9359	20.5643	19.9573
0.0673	1729	27.1148	25.8841	27.1981	25.9021	0.3397	4064	20.2342	19.7167	20.3067	19.7381
0.0673	1736	27.0898	25.8657	27.1730	25.8837	0.3627	4167	19.9717	19.4819	20.0441	19.5034
0.0675	1800	26.8668	25.7019	26.9490	25.7200	0.3781	4266	19.7909	19.3138	19.8634	19.3354
0.0677	1864	26.6838	25.5681	26.7654	25.5863	0.3831	4300	19.7320	19.2599	19.8045	19.2815
0.0681	1931	26.5027	25.4430	26.5839	25.4613	0.3980	4417	19.5631	19.1111	19.6357	19.1328
0.0685	2010	26.3045	25.3151	26.3856	25.3335	0.4107	4527	19.4259	18.9931	19.4988	19.0148
0.0691	2117	26.0177	25.1107	26.0980	25.1293	0.4222	4634	19.3078	18.8934	19.3810	18.9151
0.0697	2206	25.7925	24.9398	25.8719	24.9586	0.4330	4741	19.2020	18.8059	19.2756	18.8276
0.0700	2243	25.7030	24.8708	25.7820	24.8896	0.4431	4845	19.1057	18.7268	19.1797	18.7486
0.0704	2287	25.5962	24.7882	25.6748	24.8072	0.4528	4946	19.0131	18.6508	19.0875	18.6726
0.0711	2377	25.3842	24.6165	25.4619	24.6357	0.4624	5048	18.9217	18.5753	18.9965	18.5970
0.0720	2463	25.1840	24.4591	25.2611	24.4785	0.4718	5148	18.8303	18.4990	18.9054	18.5208
0.0730	2549	24.9889	24.2942	25.0652	24.3137	0.4812	5247	18.7376	18.4209	18.8130	18.4427
0.0742	2635	24.7996	24.1246	24.8753	24.1443	0.4907	5347	18.6423	18.3397	18.7181	18.3614
0.0756	2719	24.6150	23.9581	24.6901	23.9779	0.5002	5445	18.5431	18.2539	18.6191	18.2757
0.0764	2761	24.5244	23.8764	24.5993	23.8964	0.5099	5543	18.4382	18.1620	18.5145	18.1838
0.0766	2771	24.5026	23.8567	24.5774	23.8767	0.5198	5639	18.3253	18.0617	18.4019	18.0835
0.0783	2847	24.3371	23.7016	24.4115	23.7217	0.5301	5736	18.2007	17.9492	18.2775	17.9710
0.0804	2931	24.1609	23.5318	24.2349	23.5521	0.5407	5830	18.0590	17.8191	18.1361	17.8409
0.0830	3014	23.9881	23.3654	24.0617	23.3859	0.5520	5924	17.8916	17.6629	17.9690	17.6847

Notes. The table has the same structure and content as Table B.1, but refers to the HMHA40 model.